Brain activity reconstruction from non-stationary M/EEG data using spatiotemporal constraints

Reconstrucción de la actividad cerebral desde datos de M/EEG no estacionarios usando restricciones espacio temporales

Fily Mateos Grisales Franco

Universidad Nacional de Colombia
Faculty of Engineering and Architecture
Department of Electrical, Electronic and Computer Engineering
Manizales, Colombia
2016

Brain activity reconstruction from non-stationary M/EEG data using spatiotemporal constraints

Reconstrucción de la actividad cerebral desde datos de M/EEG no estacionarios usando restricciones espacio temporales

Fily Mateos Grisales Franco

Thesis presented as partial requirement to obtain the degree:
Master of Engineering

Advisor:
Ph.D. Germán Castellanos Domínguez
co-Advisor:
M.Sc. Juan David Martínez Vargas

Research Area:
Digital Signal Processing
Research Group:
Processing and Recognition Signal Group

Universidad Nacional de Colombia
Faculty of Engineering and Architecture
Department of Electrical, Electronic and Computer Engineering
Manizales, Colombia
2016

I'm just a link in the chain that drives this work.

Acknowledgements

Thanks to the writer of life for taking me to the right places at the right moment, because in the path traveled these places and moments have represented people, dreams, times, falls. In short, everything that has built me and visualized here.
I am especially grateful with my advisor Germán Castellanos and co-advisor Juan David because without their knowledge, experience, guide, dedication and understanding every thought and written word would be only a disorder, an incomprehension; and also, I always understood between the lines that they believed in me. Likewise, express my gratitude to all members of the Processing and Recognition Signal Group, for enriching my academic and personal life. And with great affection to that little group of friends who toured and made with me the university life.
Finally, I thank my parents, brothers, family, and friends that become family. For believing in me unconditionally and supporting me every step that I give, since they are my foundation my greatest personal achievement. I hope someday give them as much as they give me because I recognize their struggles, efforts, love in general.
For all "Gracias Totales"

Fily Mateos

This research was carried out under the projects:

- Project: Evaluación asistida de potenciales evocados cognitivos como marcador del trastorno por déficit de atención e hiperactividad (TDAH)-Código: 1119-569-3352.
- Project: Plataforma tecnológica para los servicios de teleasistencia, emergencias médicas, seguimiento y monitoreo permanente de pacientes y apoyo a los programas de prevención, Eje 2 - ARTICA-Código: 2010-100-8269.

Abstract

Magneto/Electroencephalography (M/EEG)-based neuroimaging is a widely used noninvasive technique for functional analysis of neuronal activity. One of the most prominent advantages of using M/EEG measures is the very low implementation cost and its height temporal resolution. However, the number of locations measuring magnetic/electrical is relatively small (a couple of hundreds at best) while the discretized brain activity generators (sources) are several thousand. This fact corresponds an ill-posed mathematical problem commonly known as the M/EEG inverse problem. To solve such problems, additional information must be apriori assumed to obtain a unique and optimal solution. In the present work, a methodology to improve the accuracy and interpretability of the inverse problem solution is proposed, using physiologically motivated assumptions. Firstly, a method constraining the solution to a sparse representation in the space-time domain is introduce given a set of methodologies to syntonize the present parameters. Secondly, we propose a new source connectivity approach explicitly including spatiotemporal information of the neural activity extracted from M/EEG recordings. The proposed methods are compared with the state-of-art techniques in a simulated environment, and afterward, are validated using real-world data. In general, the contributed approaches are efficient and competitive compared to state-of-art brain mapping methods.

Keywords: M/EEG, inverse problem, brain mapping, source connectivity.

Resumen

El mapeo cerebral basado en señales de magneto/electroencefalografía (M/EEG), es una técnica muy usada para el análisis de la actividad neuronal en forma no invasiva. Una de las ventajas que provee la utilización de señales M/EEG es su bajo costo de implementación además de su sobresaliente resolución temporal. Sin embargo el número de posiciones magnéticas/eléctricas medidas son extremadamente bajas comparadas con la cantidad de puntos discretizados dentro del cerebro sobre los cuales se debe realizar la estimación de la actividad. Esto conlleva a un problema mal condicionado comúnmente conocido como el problema inverso de M/EEG. Para resolver este tipo de problemas, información apriori debe ser supuesta para así obtener una solución única y óptima. En el presente trabajo investigativo, se propone una metodología para mejorar la exactitud e interpretación a la solución del problema inverso teniendo en cuenta el contexto fisiológico del problema. En primer lugar se propone un algoritmo en el cual se representa la actividad cerebral a través de un conjunto de funciones espacio-temporales dando metodologías para sintonizar los parámetros presentes. En segundo lugar, proponemos un nuevo enfoque mediante conectividad en fuentes que explícitamente incluye información espacial y temporal de la actividad neuronal extraída del M/EEG. Los métodos propuestos son comparados con métodos del estado del arte usando señales simuladas, y finalmente son validados usando datos reales de M/EEG. En general, los métodos propuestos son eficientes y competitivos en comparación a los métodos de referencia.

Keywords: EEG, problema inverso, mapeo cerebral, conectividad en fuentes.

Contents

Notation

Variables and Functions

$\boldsymbol{J}$	Brain activity
$\widehat{\boldsymbol{J}}$	Estimated brain activity
$\boldsymbol{Y}$	M/EEG data
$\boldsymbol{L}$	Lead field matrix
$\boldsymbol{\Xi}$	M/EEG measurement noise
D	Number of dipoles
C	Number of electrodes
T	Number of time samples
M	Number of regularized penalty functions
S	Number of basis functions
$\boldsymbol{Q}$	A priori covariance matrix of brain activity
$\boldsymbol{Q}_{\Xi}$	M/EEG measurement noise covariance matrix
λ	Regularization parameter
λ_s	Spatial regularization parameter
λ_t	Time regularization parameter
$\lambda_{\max}$	Spatial critical regularization parameter
ρ	Ideal residual norm
$\boldsymbol{I}_n$	Identity matrix of size n
$\boldsymbol{\Delta}$	Spatial Laplacian operator
$\boldsymbol{\Phi}$	Spatial basis
$\boldsymbol{H}$	Weights of the spatial basis
$\boldsymbol{\mathcal{G}}$	Green function
$\boldsymbol{P}$	Vertex-edge incident matrix

ε_s	Earth-Movers Distance
ε_t	Temporal Accuracy Index
r	ROI time course
γ	Magnitude Square Coherence
$\mathbf{\Gamma}$	Connectivity matrix
$\boldsymbol{\Upsilon}$	Feature representation matrix

Mathematical Operators

$\|\| \cdot \|\|_F$	Frobenius norm
$\|\| \cdot \|\|_p$	L_p-norm
$\|\| \cdot \|\|_\infty$	L_∞-norm
$\langle \cdot \rangle$	Matrix inner product

Abbreviations

EEG	Electroencephalography
MEG	Magnetoencephalography
SPECT	Single Photon Emission Computer Tomography
PET	Position Emission Tomography
fMRI	functional Magnetic Resonance Imaging
ERP	Evoked Potential Responses
IP-M/EEG	M/EEG inverse problem
MNE	Minimum Norm Estimate
LORETA	Low Resolution Tomography
LASSO	Least Absolute Shrinkage and Selection Operator
MCE	Minimum Current Estimate
ARD	Automatic Relevance Determination
GS	Greedy Search
MSP	Multiple Sparse Priors

S-FLEX	Sparse Basis Field Expansion
AR	Auroregressive
SVD	Singular Value Decomposition
MAP	Maximum A Posteriori
DSC	Dinamic Sparse Coding
FISTA	Fast Iterative Shrinkage-thresholding algorithm
SNR	Signal to noise ratio
ADHD	Attention-deficit/Hyperactivity disorder
NAC	Neuropsychological Assessment of Children
DEAP	Dataset for emotion analysis using physiological signals
SAM	Self-assessment manikins
ROI	Region of Interest
MSC	Magnitude Square Coherence
SVM	Support Vector Machine
ITL	Information Theoretic Learning

1 Preliminaries

1.1 Introduction

The human brain study is an important and exciting area due to its complexity and functionality. Consequently, a better understanding of these facts may lead to the treatment of brain diseases or even to interpret the human cognitive processes. So, the principal aim is to study the brain behavior to identify areas corresponding to certain pathologies or cognitive processes (i.e., information extraction in the spatial domain) and at the same time, identifying and characterizing temporal brain activation patterns, to explain how the brain areas are related to each other and how the brain works as a whole.
Nevertheless, one of the problems to be faced in the brain study is information sensing and extraction. Hence, Noninvasive techniques for functional analysis of neuronal activity have recently been developed to give the best interpretation of electrophysiological, hemodynamic, metabolic and neurochemical processes that describe the functionality of the human brain associated with disease states, alterations, or human behavior [1]. Such non-invasive medical techniques include Single Photon Emission Computer Tomography (SPECT), Positron Emission Tomography (PET), functional Magnetic Resonance Imaging (fMRI), Magnetoencephalography (MEG) and Electroencephalography (EEG) [2]. In any case, these techniques include variant resolution measures, both in time and space, depending on the particular application. Thus, the fMRI has a great spatial resolution, allowing to precisely identify active areas related to certain brain states [3]. Nevertheless, such method is expensive and do not offer a good temporal resolution. On the other hand, MEG and EEG are techniques with high temporal but low spatial resolution. Particularly, EEG is preferable in our conditions mainly because of its very low implementation cost compared to other options for medical image analysis. As a result, the EEG signals have wide applications in the direct and real-time monitoring of brain activity, for instance identifying and analyzing neural rhythms, Evoked Potential Responses (ERPs), epileptic spikes, among other applications.
The reconstruction of neural activity from M/EEG recordings begins with the acquisition of the signal through the electrodes placed on the scalp. Notice that M/EEG recordings also have spatial information because they are usually measured over the entire head surface, consequently, they have been used as a neuroimaging tool. Thereby, possible current sources within the brain are associated with the sensor measurements using a structural model of the head, whose complexity usually affects the reconstruction of neuronal activity [4]. Then, the acquired M/EEG recordings and the defined head model are used to reconstruct the

sources of neuronal activity [5]. However, this step leads to an issue that is the estimation of the location and distribution of these current sources responsible for the electromagnetic activity in the brain from the acquired information. Because the number of locations measuring magnetic/electrical activity is relatively small (a couple of hundreds at best) while the discretized brain activity generators (sources) reaches as much as several thousand. This fact corresponds an ill-posed mathematical problem due to the number of variables (parameters to be determined) is larger than the number of known parameters (available information) resulting in a not unique solution [5]. This problem is commonly referred to as the M/EEG inverse problem (IP-M/EEG).

In the IP-M/EEG, the estimation model could be assumed as a linear relationship between the M/EEG measurements on the scalp (M/EEG potential vectors) with current sources within the brain (current density vectors) through a transformation operator (field electric conduction array), adding the inherent noise in the M/EEG signals (noise vector). This estimation model generates non-uniqueness of solutions because it is ill-posed, i.e., small variations in the measured data lead to solutions with completely different configurations of the current sources. To reduce this effect of non-uniqueness is necessary that more information about neural structure and dynamics are available in order to get a unique and optimal solution [5]. Thus, the model inference should be provided with more information extracted from the data itself (prior information or just the priors). This information may reflect anatomical, physical and/or mathematical properties of the currents within the brain.

Current solution methods of the IP-M/EEG are: dipole solutions, which assume current densities as a set of current dipoles; and distributed inverse solutions, assuming that the current density is widely distributed in the brain. The first model is appropriate in cases where it is presumed that small surface areas are activated, but the estimation is biased by the number of dipoles arranged in the solution. The latest solution model has been more widely employed in tasks that assume abrupt and sparse neuronal activity [6]. The different methods of solution proposed for the distributed model usually can be interpreted as a penalized regression framework, in which the estimated current densities corresponds to the minimization coefficients of a penalized least squares regression and the penalty term varies depending on the prior assumptions.

Mainly, these assumptions are considered in the spatial (by inserting an a priori covariance matrix) or temporal (through state space models) domains.

In the first case (spatial constraints), classic mapping strategies are based on the simplest *Minimum Norm Estimates (MNE)* [7], and/or the spatiality smoothest like *LOw REsolution TomograAphy (LORETA)* [8]. Such methods are implemented using L_2-norm penalty terms, and they choose the covariance matrix as the identity matrix and the discrete Laplacian operator, respectively. Although these conventional mapping methods have benefits in implementation and robustness to noise, they do not take into account physiologically meaningful properties of the brain activity and make assumptions that tend to blur activity across the cortex, resulting in diffused solutions even for focal sources, causing the presence of

so-called ghost sources [9]. On the other hand, it has also been argued that small fractions of the brain should be consistently activated, so methods based on the minimization of L_1-norm that assuming sparsity in the spatial domain have been proposed [10, 5], but while being physiologically motivated, these solutions suffer of instability and spatial scattering [11].

To overcome these issues, some approaches assume brain activity represented by a small-sparse set of spatial basis functions (termed spatial blobs or patches). Thus, brain activity is represented as linear combination of several predefined spatial patches. The following patch-based approaches are the most representative: *Automatic Relevance Determination (ARD)*, *Greedy Search (GS)*, *Multiple Sparse Priors (MSP)* [12, 13], *Sparse Basis Field Expansion (S-FLEX)* [11]. However, the spatial distribution of those methods states that the active brain patches remain the same throughout the entire solution interval [9]. Such an assumption is far from being totally realistic in many practical tasks where brain activity may have strong spatiotemporal dynamics and non-stationarities [14].

On the other hand, prior information can also be included in the form of temporal constraints describing the temporal dynamics of neural activity. In this regard, from a general point of view, two approaches have been presented: The first one deals with the inclusion of autoregressive (AR) models to explicitly constraint estimated brain activity time series. The most naive approach (it can be seen as the time-domain equivalent of LORETA) is to model brain activity through a random walk model [15, 16], thereby, encouraging the smoothest time series. A more elaborate approach was introduced in [17] and further analyzed in [18], here, a second order linear model explicitly holding temporal resonance is used. However, sophisticated tuning along with an increased computational burden make those methods infeasible when the number of brain activity generators becomes large enough.

In contrast, the second approach to include apriori information in the time domain is to automatically identify the main dynamics of available data and use such components as implicit constraints. For example, in [19, 20] the temporal components are identified through an SVD decomposition of the temporal covariance matrix of the data and the solution is found using only the most relevant time-domain components. Nevertheless, the correct identification of the brain dynamics highly depends on of the noise power. Consequently, there is a growing necessity for developing methods of neural activity reconstruction including spatial prior information adjusted to the non-stationary structure of EEG data.

On the last decade a 'paradigm shift' has appeared in functional brain imaging [21]. Nowadays researchers seek to elucidate spatial patterns of temporal covariation between brain regions based on noninvasively obtained electrophysiological measures of neural activity, instead of studying the activity and function of brain regions in isolation [22, 23]. Nevertheless, the interpretation of estimated connectivity from sensor level recordings (M/EEG) is not straightforward, as effects of field spread severely corrupt these recordings. A partial solution to these difficulties is to apply connectivity methods to brain sources reconstructed from M/EEG signals [24, 25, 26, 22, 27, 23, 28]. However, the spatiotemporal properties of the employed inverse method critically bound the source connectivity assessment and

interpretation [29].
From this review, two main problems must be addressed: *i*) How to properly include and combine spatial and temporal penalties in the solution of the M/EEG inverse problem, and *ii*) How to use such enhanced brain activity estimation to improve further learning stages, specifically functional connectivity analysis.

1.2 Objectives

1.2.1 General Objective

To develop a framework that improves the accuracy and interpretability of the brain activity reconstruction using constraints with spatial coherence considering at the same time the non-stationarity of M/EEG.

1.2.2 Specific Objectives

1. To develop a methodology that allows including spatial and temporal constraints related to the dynamics of the brain activity, to get the neural activity reconstruction with temporal homogeneity and spatial sparsity.

2. To develop an optimization strategy for tuning the parameters present in the spatial-temporal restrictions of linear regression methods for mapping the neural activity.

3. To develop a methodology of source connectivity analysis that allows estimating connectivity measures from remaining parameters in time.

1.3 Outline

The present research work can be read as follows: In Chapter 2 a review of the M/EEG inverse problem solution is presented. Chapter 3 is devoted to introducing a methodology to solving the M/EEG inverse problem including spatiotemporal constraints. Finally, in Chapter 4, a source connectivity methodology is presented based on the characteristics of the source estimation method introduced.
In Chapter 3, we present a new method that allows including spatial and temporal constraints directly in the source space. Moreover, the spatial accuracy is improved by including a basis set describing smooth localized areas of potentially active brain regions. Consequently, the reconstruction of non-stationary brain activity reaches a trade-off between temporal and spatial resolutions controlled by different tunning methodologies propose. To validate the proposed method, we use two simulated database and two real databases and compare with methods establish in the state-of-art.

In Chapter 4, we present a methodology of source connectivity analysis that exploits the most remarkable features of the proposed brain activity estimation approach. To this end, the methodology explicitly including spatiotemporal information of the neural activity extracted from M/EEG recordings, carrying out three stages what includes the Region of Interest (ROI) identification, estimation of ROI time courses, and finally the functional connectivity measure computed between a pair of ROIs. The proposed source connectivity methodology is validated discriminating emotional stages.
Finally, general conclusions and main contributions of this research work are presented in Chapter 5.

1.4 Academic Discussion

J. D. Martínez-Vargas, F. M. Grisales-Franco, E. Giraldo-Suarez, G. Castellanos-Dominguez. "Enhanced spatio-temporal resolution using Dynamic Sparse Coding for solving the EEG inverse problem", submitted to *Journal of Neural Engineering - IOPscience.* 2016.

Juan-David Martinez-Vargas, Fily-Mateos Grisales-Franco, Gregor Strobbe, Pieter van Mierlo, German Castellanos-Dominguez. "Assessment of dynamic source connectivity using temporal constraints for localization of epileptogenic foci", submitted to *Journal: NeuroImage.* 2016.

F. M. Grisales-Franco, F. Vargas, A.A. Orozco, M.A. Alvarez, G. Castellanos-Dominguez. "Fall detection algorithm based on thresholds and residual events", in *Iberoamerican Congress on Pattern Recognition. Springer International Publishing.* November 2015, Pages 575-583.

J. D. Martínez-Vargas, F. M. Grisales-Franco, G. Castellanos-Dominguez,"Estimation of M/EEG Non-stationary Brain Activity Using Spatiotemporal Sparse Constraints", Artificial Computation in Biology and Medicine: International Work-Conference on the Interplay Between Natural and Artificial Computation, IWINAC 2015, Elche, Spain, June 1-5, 2015, Proceedings, Part I, Pages 429-438, ISBN 978-3-319-18914-7.

Castro-Hoyos, C., Grisales-Franco, F. M., Martínez-Vargas, J. D., Acosta-Medina, C. D., Castellanos-Domínguez, G. "Stationary Signal Separation Using Multichannel Local Segmentation", in *Iberoamerican Congress on Pattern Recognition. Springer International Publishing.* November 2014, Pages 183-190.

F. M. Grisales-Franco, C., J. D. Martínez-Vargas, L.M. Sepulveda-Cano, J. D., G. Castellanos-Dominguez. "Signal Phonocardiographic Analysis based on Wavelet Packets to Detect Heart Murmurs.",*Simposio de Tratamiento de Señales, Imágenes y Visión Artificial STSIVA.* 2011.

2 MEG/EEG inverse problem formulation

2.1 Introduction

In this chapter, an illustrative explanation of several methods for solving the M/EEG inverse problem is introduced. In the first part we present the formulation of the inverse problem followed by the explication of different methods that select the prior information in the spatial domain, discriminated as follows: methods with simple spatial structure like *Minimum Norm Estimation (MNE)* and *Low-Resolution Brain Electromagnetic Tomography (LORETA)*, methods with sparse spatial structure like the *Least Absolute Shrinkage and Selection Operator (LASSO)*, and finally more elaborated methods based on smooth and focal spatial structure known as *Multiple Sparse Priors (MSP)* and *Sparse Basis Field Expansion (S-FLEX)*.
The mathematical framework presented here is focused on solving the M/EEG inverse problem on a single trial, subject, and modality, with the objective of providing a background for the remaining of this thesis. Group based inversions, fusing modalities, introduction of functional MRI (fMRI) data, and advanced de-noising techniques are out of the scope of this work and have been well reviewed elsewhere [30, 31, 32].

2.2 Formulation of the MEG/EEG inverse problem

With the aim to represent the electromagnetic field magnitude measured by the scalp, we assume the following linear model [1]:

$$\boldsymbol{Y} = \boldsymbol{L}\boldsymbol{J} + \boldsymbol{\Xi}, \tag{2-1}$$

where $\boldsymbol{Y}\in\mathbb{R}^{C\times T}$ is the M/EEG data measured by $C\in\mathbb{N}$ sensors at $T\in\mathbb{N}$ time samples, $\boldsymbol{J}\in\mathbb{R}^{D\times T}$ is the amplitude of $D\in\mathbb{N}$ current dipoles (or sources), distributed through the cortical surface with a fixed orientation perpendicular to it, and $\boldsymbol{L}\in\mathbb{R}^{C\times D}$ (commonly termed *lead field matrix*) is a gain matrix representing the relationship between the dipoles and M/EEG data. Also, the noisy nature of the M/EEG recordings is explicitly taken into account through the error matrix $\boldsymbol{\Xi}\in\mathbb{R}^{C\times T}$, where the uncorrelated noise is assumed to be Gaussian with zero mean and covariance matrix $\boldsymbol{Q}_{\Xi}\in\mathbb{R}^{C\times C}$.

This linear model in Eq. (2-1) is ill-posed because the transformation operator $\boldsymbol{L}$, (which physically corresponds to the conduction array of the field electric) is non-invertible and the dipoles outnumber the sensors ($D \gg C$), consequently, small variations in the measured data $\boldsymbol{Y}$ lead to solutions with completely different configurations of the current sources $\boldsymbol{J}$. Therefore, the M/EEG inverse problem may be formulated as a maximum a-posteriori (MAP) estimation procedure by finding the most probable estimation $\hat{\boldsymbol{J}}$ regarding to the measured M/EEG data and *a priori* considerations. Although there are several distributed inverse solutions by this MAP through the minimization of a particular cost function, a general formulation of this problem as a *Multiple Penalized Least Squares Model* is presented as follows [6]:

$$\widehat{\boldsymbol{J}} = \underset{\boldsymbol{J}}{\operatorname{argmin}}\{||\boldsymbol{Y} - \boldsymbol{L}\boldsymbol{J}||_F^2 + \sum_{m \in M} \lambda_m \Theta_m(\boldsymbol{J})\}, \tag{2-2}$$

where $\{\lambda_m \in \mathbb{R}^+\}$ is the regularization parameter set, $\{\Theta_m(\boldsymbol{J}) \in \mathbb{R}\}$ is a penalty function set, and notation $||\cdot||_F$ stands for the Frobenius norm. Note that the first quadratic term in Eq. (2-2) is the log-likelihood, and the second term holds all prior information through the $M \in \mathbb{N}$ regularized penalty functions.

2.3 Selection of prior information in the spatial domain

2.3.1 Simple spatial structure

Several inverse solutions are found through the selection of the priors (second term in Eq. (2-2)), which are generally based on convex functions that carry to convex optimization problems, given that they include benefits such as a global (unique) minimum, and reliable and efficient numerical solution methods [33]. So, several of the most common inverse solutions are based on the convex function formed for the squared Frobenius norm establishing the following minimization problem:

$$\underset{\boldsymbol{J}}{\operatorname{argmin}}\{||\boldsymbol{Y} - \boldsymbol{L}\boldsymbol{J}||_F^2 + \lambda||\boldsymbol{Q}\boldsymbol{J}||_F^2\}, \tag{2-3}$$

this functional Eq. (2-3) known in the linear regression field as *Ridge Regression*, is interpreted as a penalized least squares regression with the penalty restriction (prior) represented as a Gaussian distribution with zero mean and covariance matrix $\boldsymbol{Q}$, which admits a closed-form solution to estimate the brain activity $\widehat{\boldsymbol{J}}$, as follows:

$$f(\boldsymbol{Q}, \boldsymbol{Y}) : \widehat{\boldsymbol{J}} = \boldsymbol{Q}\boldsymbol{L}^\top(\boldsymbol{Q}_{\boldsymbol{\Xi}} + \boldsymbol{L}\boldsymbol{Q}\boldsymbol{L}^\top)^{-1}\boldsymbol{Y}. \tag{2-4}$$

Here, different prior assumptions are given by choice of $\boldsymbol{Q}$ greatly affecting the solution. Therefore, its selection is an issue of great interest.

Into the multiple forms to select the prior source covariance matrix $\boldsymbol{Q}$ there are two important and popular cases with a simple spatial structure known as *Minimun Norm Estimated (MNE)* [7] and *Low Resolution Electromagnetic Tomographic (LORETA)* [8]. In the simplest approach, MNE minimizes the overall power of the sources assuming that all dipoles have approximately the same prior variance and no covariance, by defining $\boldsymbol{Q} = \boldsymbol{I}_D$. And with a more elaborate approach, LORETA explicitly enforces spatial smoothness of the sources assuming that neighboring voxels should be similarly active, by defining $\boldsymbol{Q} = \left(\Delta^\top \Delta\right)^{-1}$, being $\Delta \in \mathbb{R}^{D \times D}$ the spatial Laplacian operator.

2.3.2 Sparse spatial structure

These conventional methods have benefits in implementation and robustness to noise, but they do not take into account the natural assumption that only a few brain regions are typically active during a cognitive task [9]. Consequently, methods which can produce sparsity in the spatial domain and more concentrated solutions have been proposed. These methods usually based on their L_1-norm, assume the prior information according to the Laplace distribution with zero mean and identity matrix covariance with a non-quadratic penalty function of the coefficients $\boldsymbol{J}$, This assumption is equivalent to fix $\Theta(\boldsymbol{J}) = \|\boldsymbol{J}\|_1$, where $\|\cdot\|_1$ is the L_1-norm. Consequently, the optimization problem in Eq. (2-2) is redefined as the *Least Absolute Shrinkage and Selection Operator (LASSO)* problem [34]:

$$\underset{\boldsymbol{J}}{\operatorname{argmin}}\{||\boldsymbol{Y} - \boldsymbol{L}\boldsymbol{J}||_F^2 + \lambda\|\boldsymbol{J}\|_1\}, \tag{2-5}$$

Also, know as *Minimun Current Estimate (MCE)* by the M/EEG inverse problem [35]. The LASSO reduces the variability of the estimates by shrinking the sources and at the same time produces interpretable models by shrinking some sources to exactly zero, i.e., a sparse estimation.

2.3.3 Smooth and focal spatial structure

Although the above methods are motivated by neurophysiological arguments, in practice these solutions have undesirable and non-realistic results of spatial neural activity, such as: the smooth solutions tend to estimate spatially blurred sources that spread over a considerable part of the brain appearing ghosts sources; and sparse solutions tend to estimate unstable and scattered sources around the real sources [36, 11, 5]. So, to better manage localization of active sources, more elaborate state-of-art methods [12, 11] have assumed that the brain activity can be expressed through a small/sparse set of space basis functions describing smooth localized patches of potentially active brain regions, as follows:

Multiple Sparse Priors (MSP)

Making more flexible the definition of $\boldsymbol{Q}$ in Eq. (2-4), as discussed in [12, 13], the matrix $\boldsymbol{Q}$ is expressed in terms of a linear combination of a fixed, but known set of components contained in the columns of a given matrix $\boldsymbol{\Phi}\in\mathbb{R}^{D\times S}$ as follows:

$$\boldsymbol{Q} = \sum_{i\in S} h_i \text{Diag}(\boldsymbol{\Phi}(\cdot, i)) \tag{2-6}$$

where $\text{Diag}(\boldsymbol{\Phi}(\cdot, i))\in\mathbb{R}^{D\times D}$ is a diagonal matrix formed by the $i-$th column of $\boldsymbol{\Phi}$ and holding to a given prior component; $h_i\in\mathbb{R}$ is a weithing hyperparameter, which is commonly calculated based on the M/EEG data covariance [13]. Given the brain activity is expected to happen in sparse and locally smooth brain areas (referred as spatial coherence), the set $\boldsymbol{\Phi}$ can be extended by defining each column of $\boldsymbol{\Phi}$ as a potentially active cortex area (termed cortical or spatial patch), as illustrated in Fig. **2-1**. The use of an extended set $\boldsymbol{\Phi}$ that is formed by a set of cortical patches is the main idea behind *Automatic Relevance Determination (ARD)*, *Greedy Search (GS)*, and by extension the *Multiple Sparse Priors (MSP)*, presented in [12] and explored to a greater extent in [37, 13]. In all of these algorithms, the estimation problem is further constrained by assuming that a small set of spatial patches is enough to explain observed data, i.e., there is a sparsity assumption in the estimation of the coefficients set $\{h_i\}$ which is achieved by assuming that such parameters follow the Laplacian distribution.

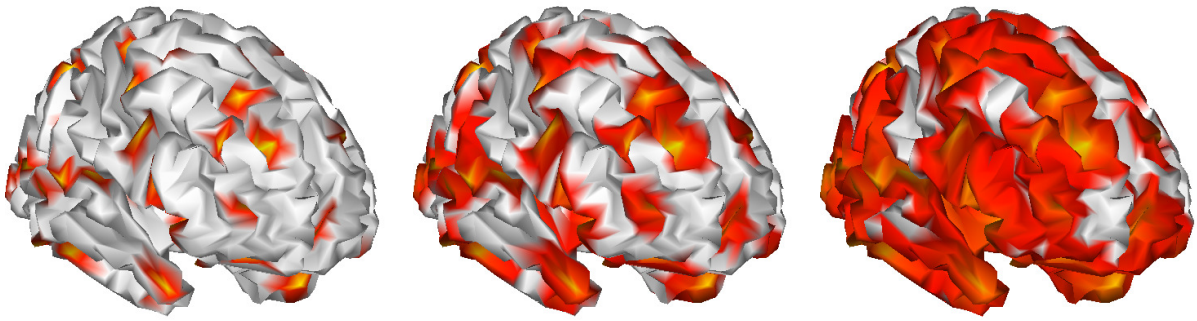

(a) Small. (b) Medium. (c) Large.

Figure **2-1**: Example of spatial patches, with different sizes, used in ARD/GS/MSP and S-FLEX. Each column of $\boldsymbol{\Phi}$ corresponds to a single cortical patch.

Sparse Basis Field Expansion (S-FLEX)

From another perspective the *Sparse Basis Field Expansion (S-FLEX)* algorithm is developed in [11], where the current density is expressed as a linear combination of locally smooth,

but spatially confined spatial basis functions:

$$\boldsymbol{J} = \boldsymbol{\Phi}\boldsymbol{H}, \tag{2-7}$$

where $\boldsymbol{H} \in \mathbb{R}^{S \times T}$ contains the weightings coefficients that are assumed to have a Laplacian prior distribution. According to the aforementioned representation, and to obtain spatially sparse solutions, the following objective function is derived:

$$\underset{\boldsymbol{H}}{\operatorname{argmin}}\{||\boldsymbol{Y} - \boldsymbol{L}\boldsymbol{\Phi}\boldsymbol{H}||_F^2 + \lambda\|\boldsymbol{H}\|_{1,2}\} \tag{2-8}$$

where the notation $\|\cdot\|_{1,2}$ stands for the $L_{1,2}$-norm that is the L_1-norm grouping each vector dipole component under the L_2-norm to avoid orientation bias [11].
Once the matrix $\boldsymbol{H}$ has been estimated, then the neural activity is recovered by using Eq. (2-7). Furthermore, temporal inconsistencies produced by instantaneous S-FLEX solution that assumes M/EEG observations as independent at each time sample, temporal coherence (smooth time series) may be improved by accepting activation of the same brain areas during the entire M/EEG segment. Bearing this in mind, Eq. (2-8) is rewritten to group each dipole time series under the $L_{1,2}$-norm, considering that brain activity remains stationary for the whole analyzed time windows, as usually assumed by brain mapping methods [9, 5], However, it is commonly accepted that brain activity has non-stationary nature. Therefore, stationarity assumption may hinder brain mapping accuracy.

3 Reconstruction of neural activity from M/EEG data using dynamic spatiotemporal constraints

3.1 Introduction

In this chapter, the spatial and temporal dynamics inherent to neural processes are considered within the inverse problem solution framework, based on the assumption that brain activity appears in localized brain regions that can vary along time, yielding spatial and temporal non-stationary activity. Therefore, we propose a constrained M/EEG inverse solution namely *Dynamic Sparse Coding (DSC)*, based on the fused lasso penalty, first introduced in [38]. The DSC reconstructs the brain activity as dynamic small and locally smooth spatial patches, leading to a solution with spatial coherence, but considering at the same time the non-stationarity of M/EEG recordings.

We validate the proposed approach in two different ways: *i*) Using artificial M/EEG data when we have previous knowledge of spatial and temporal signal dynamics, simulating event-related potential (ERP) and epileptic seizures onset. And *ii*) Using real M/EEG data, particularly we use two databases one with relation to the attention-deficit/hyperactivity disorder (ADHD), and other based on emotions analysis using physiological signals. In the first, the task is to localize the generators of visual and auditory evoked potentials recorded during an oddball experiment and in the second the task is the localization of emotion related brain activity. As a result, the proposed DSC is a promising method for improving the accuracy of brain activity reconstruction with spatial coherence and temporal homogeneity.

3.2 Methods

3.2.1 M/EEG inverse problem

To represent the electromagnetic field magnitude measured by the scalp, we assume the following linear model [1]:

$$\boldsymbol{Y} = \boldsymbol{L}\boldsymbol{J} + \boldsymbol{\Xi}, \tag{3-1}$$

where $\boldsymbol{Y}\in\mathbb{R}^{C\times T}$ is the M/EEG data measured by $C\in\mathbb{N}$ sensors at $T\in\mathbb{N}$ time samples, $\boldsymbol{L}\in\mathbb{R}^{C\times D}$ is the *lead field matrix* that represents the relationship between D distributed sources inside the brain and the sensor M/EEG activity, $\boldsymbol{J}\in\mathbb{R}^{D\times T}$ is the cortical source activity, and $\boldsymbol{\Xi}\in\mathbb{R}^{C\times T}$ is the observation noise measured with spatial covariance $\boldsymbol{Q}_{\Xi}\in\mathbb{R}^{C\times C}$. With the aim to estimate the source amplitude $\boldsymbol{J}$ through the minimization of a particular cost function, we present a general formulation of this problem as a Multiple Penalized Least Squares Model as follows:

$$\widehat{\boldsymbol{J}} = \underset{\boldsymbol{J}}{\operatorname{argmin}}\{||\boldsymbol{Y}-\boldsymbol{L}\boldsymbol{J}||_F^2 + \sum_{m\in M}\lambda_m\Theta_m(\boldsymbol{J})\}, \tag{3-2}$$

where $\{\lambda_m\in\mathbb{R}^+\}$ is the regularization parameter set, $\{\Theta_m(\boldsymbol{J})\in\mathbb{R}\}$ is a penalty function set, and notation $||\cdot||_F$ stands for the Frobenius norm. Note that the first quadratic term in Eq. (3-2) is the log-likelihood, and the second term holds all prior information through the $M\in\mathbb{N}$ regularized penalty functions. Several inverse solutions are found by the choice of the prior information encoded by constraints established in the model.

3.2.2 DSC for encouraging sparsity and temporal homogeneity

In practice, methods promoting at the same time more focal solutions and spatially smooth current distributions yield a better source reconstruction than other approaches, which are either purely smoothed or grounded only on sparse representations [39]. Consequently, the current density can be expressed as a linear combination of $S\in\mathbb{N}$ locally smooth, but spatially confined spatial basis functions $\boldsymbol{\Phi}\in\mathbb{R}^{D\times S}$, as described below:

$$\boldsymbol{J} = \boldsymbol{\Phi}\boldsymbol{H}, \tag{3-3}$$

where $\boldsymbol{H}\in\mathbb{R}^{S\times T}$ are the weights computed for the spatial basis set.
In Eq. (3-3), each column of the spatial basis matrix draws a single distributed pattern with compact spatial support. In particular, the spatial extent of each element is extracted from a smoothing operator derived from the Green function as $\boldsymbol{\mathcal{G}}=\exp\{\sigma\boldsymbol{\Lambda}\}$, where the matrix $\boldsymbol{\Lambda}\in\mathbb{R}[0,1]^{D\times D}$ encodes all neighborhood relationships between the nodes of the cortical mesh belonging to the solution space that is delimited by the spatial extent of the active regions $\sigma\in\mathbb{R}^+$ [40].
In the cases when the spatial profile of the source activity of interest changes within a given analysis window, the non-stationary source activations can be modeled by enforcing a temporal structure over the set of parameters $\boldsymbol{H}$. Consequently, we include both, spatial and temporal, constraints through the following regularized penalty function:

$$\Theta(\boldsymbol{J},\lambda_s,\lambda_t) = \lambda_s||\boldsymbol{H}||_1 + \lambda_t\sum_{t\in T-1}||\boldsymbol{h}_{t+1}-\boldsymbol{h}_t||_1 \tag{3-4}$$

where λ_s and $\lambda_t\in\mathbb{R}^+$ are the spatial and temporal regularization parameters, respectively, and vector $\boldsymbol{h}_t\in\mathbb{R}^{C\times 1}$ holds the t-th column of $\boldsymbol{H}$. Notation $||\cdot||_p$ stands for the L_p-norm.

As a result, the objective function takes the form:

$$\widehat{\boldsymbol{H}} = \underset{\boldsymbol{H}}{\operatorname{argmin}}\{||\boldsymbol{Y} - \boldsymbol{L}\boldsymbol{\Phi}\boldsymbol{H}||_F^2 + \lambda_s||\boldsymbol{H}||_1 + \lambda_t \sum_{t\in T-1} ||\boldsymbol{h}_{t+1} - \boldsymbol{h}_t||_1\}, \tag{3-5}$$

Note that the sparseness is encouraged by the first penalty term that assigns a large cost to matrices with the large absolute values, and thus effectively shrinking elements towards to zero. This situation means that just a few basis of the spatial dictionary will explain the main brain activity. In turn, the second penalty term encourages temporal homogeneity by penalizing the difference between consecutive time points, yielding a smooth solution over time. Therefore, the estimation of the neural activity in Eq. (3-3) is accomplished as follows:

$$\boldsymbol{J} = \boldsymbol{\Phi}\widehat{\boldsymbol{H}} \tag{3-6}$$

3.2.3 Optimization strategy of the regularized penalty function

Generally speaking, the high-dimensional and large scale problem posed in Eq. (3-5) is convex. However, this optimization task is not trivial because the non-smooth penalty function introduced in Eq. (3-4). Consequently, to reformulate the non-smooth penalty term, we make use the smooth proximal gradient algorithm that allows rewriting the fusion penalty term using an introduced vertex-edge incident matrix $\boldsymbol{P}\in\mathbb{R}^{T\times(T-1)}$, encoding the signal structure as follows [41]:

$$\sum_{t\in T-1} ||\boldsymbol{h}_{t+1} - \boldsymbol{h}_t||_1 = ||\boldsymbol{H}\boldsymbol{P}||_1.$$

Furthermore, by making $\widetilde{\boldsymbol{P}}=\lambda_t\boldsymbol{P}$, the temporal regularization parameter λ_t is also included into the term as $||\boldsymbol{H}\widetilde{\boldsymbol{P}}||_1$.
With the purpose of further computation of the smooth proximal gradient, we rewrite the overall penalty relying on the fact that the dual norm of the entry-wise matrix L_∞ is the L_1-norm, yielding:

$$||\boldsymbol{H}\widetilde{\boldsymbol{P}}||_1 \equiv \underset{||\boldsymbol{A}||_\infty\leq 1}{\operatorname{argmax}}\langle \boldsymbol{A}, \boldsymbol{H}\widetilde{\boldsymbol{P}}\rangle, \tag{3-7}$$

where $\boldsymbol{A}\in\mathbb{R}^{S\times(T-1)}$ is an auxiliary matrix associated with $||\boldsymbol{H}\widetilde{\boldsymbol{P}}||_1$, $\langle\cdot\rangle$ denotes the matrix inner product, and $\|\cdot\|_\infty$ is the matrix entry-wise L_∞-norm, defined as the maximum absolute value of all entries of the matrix.
Nonetheless, the formulation of the penalty in Eq. (3-7) does not provide an enough smooth function over $\boldsymbol{H}$. Aiming to have an adequately smooth approximation of Eq. (3-4), we propose the following auxiliary function that is strongly convex [42]:

$$f_\mu(\boldsymbol{H}) = \underset{||\boldsymbol{A}||_\infty\leq 1}{\operatorname{argmax}}\{\langle \boldsymbol{A}, \boldsymbol{H}\widetilde{\boldsymbol{P}}\rangle - \mu d(\boldsymbol{A})\} \tag{3-8}$$

where $\mu \in \mathbb{R}^+$ is a smoothness parameter and $d(\boldsymbol{A}) \equiv \frac{1}{2}\|\boldsymbol{A}\|_F^2$ is an arbitrary smooth strongly-convex function. From the Nestrov's theorem, it follows that $f_\mu(\boldsymbol{H})$ is convex and continuously differentiable in $\boldsymbol{H}$, i.e., $f_\mu(\boldsymbol{H})$ is smooth and $\nabla f_\mu(\boldsymbol{H})$ is Lipchitz continuous, so that the gradient of $f_\mu(\boldsymbol{H})$ with respect to $\boldsymbol{H}$ takes the following form [43]:

$$\nabla f_\mu(\boldsymbol{H}) = \widehat{\boldsymbol{A}}\widetilde{\boldsymbol{P}}^\top \tag{3-9}$$

where $\widehat{\boldsymbol{A}}$ is the optimal solution for $\boldsymbol{A}$ obtained in Eq. (3-8) and expressed like $\widehat{\boldsymbol{A}}=\mathcal{S}\{\boldsymbol{H}\widetilde{\boldsymbol{P}}/\mu\}$, $\mathcal{S}\{\cdot\}$ is the shrinkage operator that is defined for each entry $\xi \in \mathbb{R}$ as:

$$\mathcal{S}\{\xi\} = \begin{cases} \xi, & |\xi| < 1 \\ \operatorname{sgn}(\xi), & \text{otherwise} \end{cases}$$

Provided in terms of the smoothing approximation $f_\mu(\boldsymbol{H})$, the minimization problem in Eqs. (3-2) and (3-4) results in the next smooth optimization problem:

$$\widehat{\boldsymbol{J}} = \underset{\boldsymbol{H}}{\operatorname{argmin}}\{||\boldsymbol{Y} - \boldsymbol{L}\boldsymbol{\Phi}\boldsymbol{H}||_F^2 + \lambda_s||\boldsymbol{H}||_1 + f_\mu(\boldsymbol{H})\} \tag{3-10}$$

with the smooth part $\tilde{f}(\boldsymbol{H})=||\boldsymbol{Y} - \boldsymbol{L}\boldsymbol{\Phi}\boldsymbol{H}||_F^2 + f_\mu(\boldsymbol{H})$ for which the gradient in Eq. (3-9) is defined as below:

$$\nabla \tilde{f}(\boldsymbol{H}) = (\boldsymbol{L}\boldsymbol{\Phi})^\top(\boldsymbol{L}\boldsymbol{\Phi}\boldsymbol{H} - \boldsymbol{Y}) + \widehat{\boldsymbol{A}}\widetilde{\boldsymbol{P}}^\top \tag{3-11}$$

It is worth noting that the optimization of Eqs. (3-10) and (3-11) is carried out employing the *Fast Iterative Shrinkage-thresholding algorithm (FISTA)* [41].

3.2.4 Tunning of regularization parameters

As a rule, optimal model tuning poses a difficult task, becoming more complicated as the number of parameter increases. Thus, a critical issue for solving the *Dynamic Sparse Coding* is the adjustment of the spatial (λ_s) and temporal (λ_t) regularization parameters that influence the most the quality of neural activity reconstruction. To this end, we adjust their ratio, reaching a trade-off between the spatial resolution (provided by the Lasso scheme) and the temporal resolution (by the Fusion strategy). Like in [39], we study three different distributed fixed ratios λ_s/λ_t=90/30, 90/90, 30/90. For the sake of comparison, we also consider the asymptotic values: $\lambda_s \neq 0$ and λ_t=0 (only spatial regularization) and $\lambda_t \neq 0$ and λ_s=0 (only temporal regularization). With the purpose of further simplification, we use two optimization strategies, which are:

Sparsest possible solution:

In this first case, we reduce the searching set of the optimal values using the heuristic approach performed in [44] that fixes λ_s as a fraction of the critical value of $\lambda_{\max}$, i.e.,

$\lambda_s^{\text{opt}}=\beta\lambda_{\max}$, where $\beta\in[0,1]$. Thus, if $\beta=1$, the source activity $\widehat{\boldsymbol{J}}$ is filled with zeros, meaning that there are no active sources (or *the sparsest possible solution*). In the opposite case, $\beta=0$, no sparse restriction is imposed. Here, we set $\lambda_{\max}=\|\boldsymbol{Y}\|_F$ (the data magnitude), and $\beta=\alpha/\|\boldsymbol{L}^\top\boldsymbol{Y}\|_F$ with $\alpha\in[0,1]$. Finally, we use the fixed ratio λ_s/λ_t to obtain λ_t.

Residual norm criterion:

In this second case, we adjust the tradeoff between data fidelity and complexity terms in the cost functions in accordance with the *Residual norm criterion* used on [39] defined as follows:

$$\rho = \frac{||\boldsymbol{Y} - \boldsymbol{L}\widehat{\boldsymbol{J}}||_F^2}{||\boldsymbol{Y}||_F^2} \tag{3-12}$$

where $\widehat{\boldsymbol{J}}$ stated as ground truth is a different estimated brain activity derived from the data and $\rho \in \mathbb{R}^+$ is the ideal residual norm. The aim is to adjust the regularization parameters until to achieve the same average residual norm of the $\widehat{\boldsymbol{J}}$ ground truth, therefore, using the fixed ratio λ_s/λ_t the regularization parameters are iteratively calculated to get reconstructions with the closest residual norm to the ideal one in each run.

3.3 Experiments

3.3.1 Illustration

Fig. **3-1** illustrates the sparsity patterns obtained for the tested inverse methods in a simulation experiment. To this regard, a simulated EEG with 32 electrodes and 60 sources was modeled using a random lead field matrix.

To investigate to which extent our *Dynamic Sparse Coding (DSC)* based approach can achieve a compromise between the solely spatial regularization (Lasso), and the entirely temporal structure reconstruction (Fusion), we fixed several fixed ratios $\lambda_s : \lambda_t = 90 : 0$ (Lasso), $90 : 30, 90 : 90, 30 : 90, 0 : 90$ (Fusion). Syntonization of the regularization parameters is carried out with the *sparsets possible solution*. Finally, we compared our results against two state-of-art methods designed to encourage sparse solutions, namely *Multiple Sparse Priors (MSP)* [12] and *Sparse Basis Field Expansion (S-FLEX)* [11].

As expected, even MSP and S-FLEX (Fig. 3.1(c) and Fig. 3.1(b), respectively), fostered sparse patterns, neither approach was able to correctly group variables along the temporal dimension. As a consequence, these methods may accurately spatially locate the sparsity pattern but without decoding the temporal structure of the sources.

Furthermore, the sparse reconstruction -Lasso- (Fig. 3.1(d)) achieved similar results to MSP and S-FLEX, accomplishing a coherent spatial sparse pattern without any temporal structure. Moreover, the purely temporal constraint -Fusion- (Fig. 3.1(h)) does not decode any

spatiotemporal information of the reconstructed source. Apparently, the lack of spatial resolution difficult the decoding of the temporal dynamics.
Lastly, the DSC based approach accurately reconstructs the spatiotemporal patterns of the simulated activity. When the spatial regularization parameter λ_s is higher than the temporal regularization parameter λ_t (Fig. 3.1(e)), the performed reconstruction is spatially enhanced, but some temporal patterns are lost. In the opposite cases shown in Fig. 3.1(f) and Fig. 3.1(g) ($\lambda_s \leq \lambda_t$), the temporal structure of the reconstructed sources is closer to the simulation, but some blurred sources appear in the spatial domain.

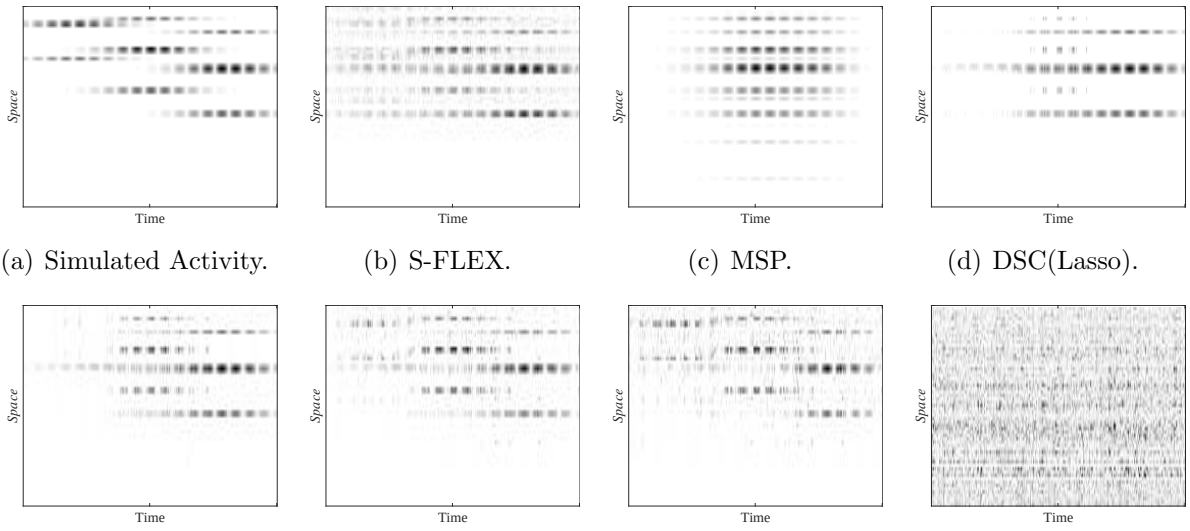

(a) Simulated Activity. (b) S-FLEX. (c) MSP. (d) DSC(Lasso).

(e) DSC(90 : 30). (f) DSC(90 : 90). (g) DSC(30 : 90). (h) DSC(Fusion).

Figure **3-1**: Time-space representation of reconstruction accomplished by various inverse methods compared to the simulated ground truth

3.3.2 Simulated EEG data

The most common approach to assessing the EEG inverse solution is the validation of a simulated set of recordings where the brain activity is already known so that the estimation quality can be objectively verified. In this regard, we created 128-channels EEG data, reproducing the pseudo-EEG at positions defined by the extended international BIOSEMI system. Validation is carried out by changing the noise conditions and testing the influence of non-stationary brain activity on the algorithm performance. Thus, two experiments are designed. In the first one (noted as *SD-1*), the activity is simulated in time-locked as usually observe in ERP studies involving one, three, and five active dipoles, respectively, having a random location in each case (see top row of Fig. **3-2**). The non-stationary EEG activity of active dipoles is generated using a set of time series created by a real Morlet wavelet that lasts one-second length, sampled at 250 *Hz*, and having the following parameters:

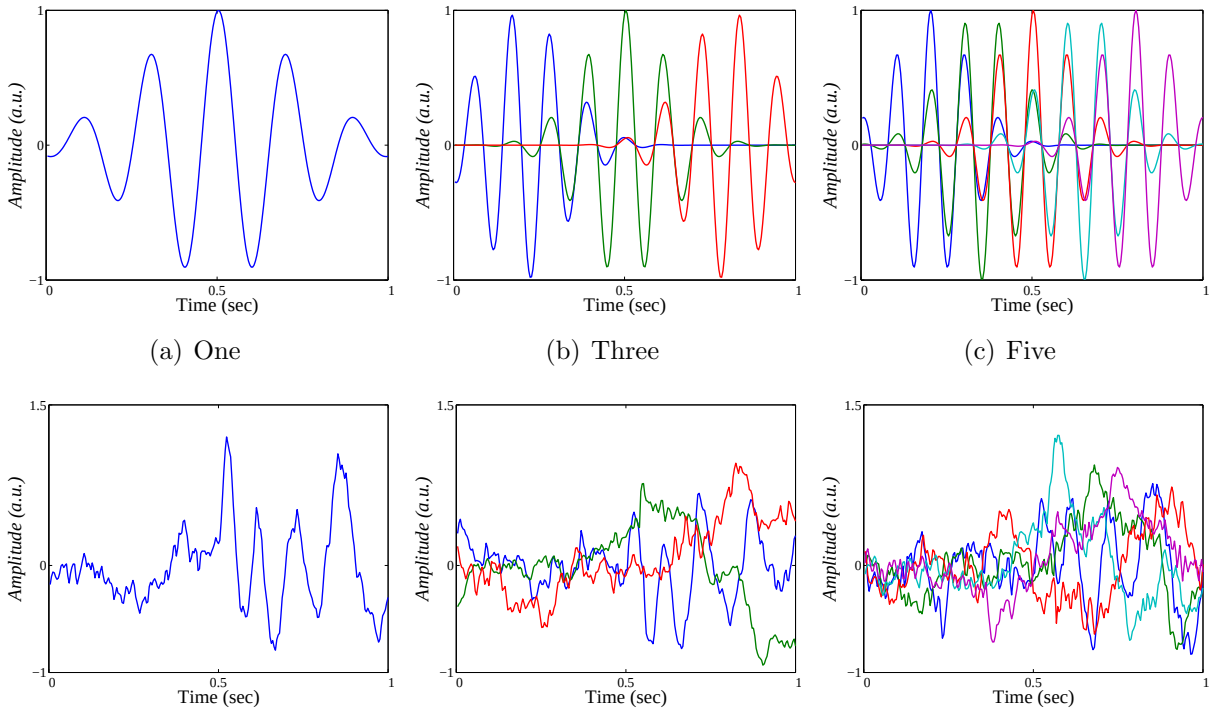

(a) One (b) Three (c) Five

(d) 0.5 (e) 0.2, 0.5, 0.8. (f) 0.2, 0.35, 0.5, 0.65, 0.8

Figure **3-2**: Example of the simulated sources for one, three, and five active dipoles: Top row displays the data for the first experiment Bottom row for the second experiment, showing the mean values fixed for each case of the simulated Morlet wavelets.

- Random central frequency with a mean of 9 Hz and standard deviation of 2 Hz, sampled from a Gaussian distribution.
- Random time shift generated by the normal distribution with standard deviation of 0.05 s and mean value selected as shown in Fig. **3-2** (bottom row).

In the second experiment that is carried out as in [45], the time-courses of active dipoles resemble an epileptic seizure onset (*SD-2*). Bottom row of Fig. **3-2** displays the simulations for one, three, and five active sources, also holding a random location. The background noise is configured to have $1/f$ spectral behavior, and the seizure activity is modeled by a sinus with a frequency content varying within the range 12 to 8 Hz, where the seizure starts at t=0.5 s, representing the onset of the epileptogenic activity. Note that the seizure is propagated among the active sources with a delay of two samples in the cases of modeling three or five sources.

Besides, we fix the location of active dipoles randomly from trial to trial. Then, simulated time courses are assigned to distributed, but neighboring nodes on the computed cortical mesh centered at the fixed random location, yielding the known activity $\boldsymbol{J}$.

The simulated source activity is mapped to EEG sensor space through a realistic volume conductor model of the human head that is obtained from a tessellated surface in the gray-white matter interface with D=8196 vertices (i.e., the number of feasible source localizations) with source orientations fixed orthogonally to the surface. Also, the lead fields are computed using a BEM volume conductor model with a mean distance between neighboring vertices adjusted to 5 mm.
Finally, we add measurement noise to achieve the following SNR levels: $-5, 0, 10$, and 15 dB. As a result, a testing set holding 30 trials for every SNR value and each simulation setting is produced.

3.3.3 Application of source reconstruction algorithms

We implement our proposal with the two strategies for syntonization of the regularization parameters explained above and compare to several inverse methods regarding their ability to reconstruct the locations and time courses of the simulated EEG activity. The considered methods are S-FLEX [11] and MSP [12]. For all tested methods, the localization is carried out using the same head model for which the data is generated. Also, the same spatial basis $\boldsymbol{\Phi}$ is employed, comprising S=512 (256 per hemisphere) that are designed to cover the entire cortical surface.
Aiming to decrease the computational burden of the optimization task, the linear model in Eq. (3-1) is reduced by the spatial projector $\boldsymbol{U}$, defined as follows:

$$\widetilde{\boldsymbol{L}} = \boldsymbol{U}^\top \boldsymbol{L},$$
$$\widetilde{\boldsymbol{Y}} = \boldsymbol{U}^\top \boldsymbol{Y},$$

where $\boldsymbol{U} \in \mathbb{R}^{C' \times C}$ holds the C' most significant singular values (spatial modes larger than some tolerance) of the lead field matrix. Note that this preprocessing stage, commonly considered for inversion schemes, does not affect the number of parameters to be estimated.

3.3.4 Evaluation of source reconstruction accuracy

The accuracy performed by each compared source reconstruction algorithm is assessed for the spatial and temporal domains by using the following measures, respectively:

Earth-Movers Distance: $\varepsilon_s \in \mathbb{R}^+$ that estimates the spatial distribution of the dipole-wise power like the rate between the neural activity to the true power of the simulated sources. Consequently, the index ε_s measures the needed effort to transform the estimated power distribution into the actual distribution by transporting the probability mass [36]. Thus, the lower the ε_s value, the better the performed reconstruction.

Temporal Accuracy Index: $\varepsilon_t \in \mathbb{R}[0,1]$, that quantifies the correlation between each of the simulated time series and the reconstructed signals at all dipoles. For each simulated source, the maximum correlation is computed across all dipoles and spatial orientations. Also, the maximum values are averaged across the simulated sources to give an average maximum correlation [39]. As a result, higher values of ε_t imply to better reconstruction of the temporal domain.

3.3.5 Localization of visual and auditory evoked potentials-related brain activity

The first real EEG data used in this study was selected from 30 children in the age ranges from 5 to 16 years belonging to two sociocultural levels (high medium and low medium). The sample was randomly selected from preschool, elementary, and secondary courses at private and public schools in the city of Manizales. Also, written permission was requested from children parents for participation in the research.
The following exclusion criteria were used: mental retardation, neurological antecedents (history of head trauma, epilepsy, and related) and psychiatric (psychiatric hospitalizations history, autism, and related) of importance according to the history data supplied by children's parents.
The *Neuropsychological Assessment of Children (NAC)* was applied to each child in two sessions of about an hour and a half. Sections of NAC were were randomly altered to monitor the effects of fatigue and order in the application of the subtests. Also, the Wechsler Intelligence Scale for Children was applied, to calculate the validity of the NAC.
Finally, experts rated the results in different cognitive and academic abilities and then a systematized database was created, including the results of children in the various tests.
As a result, 20 children in the ADHD group and 10 children in the control group were obtained.

Experimental paradigm of cognitive evoked potentials: After the neuropsychological test, we proceeded to take EEG data from all participants using an oddball paradigm, consisting of two stages, the first with visual stimuli and the second with auditory stimuli. In each condition, the stimulus lasts 130 ms, while the waiting time between two consecutive stimuli is 1 s. During each stage, the subjects had to pay attention to a pre-defined (target) stimulus and count their occurrence, ignoring the presentation of other stimuli (non-targets). The non-target stimulus was presented by 80% of the trials, while the target occurred for the 20% remaining, resulting in approximately 160 non-target stimuli and 40 target stimuli. EEG recordings were taken symmetrically using 19 electrodes with standard international system positions 10-20. Data were sub-sampled at 250 Hz and segmented in 1 s epochs. The resulting epochs were averaged separately for each subject, stimulation condition targets and non-targets.

Source localization and statistical analysis: The DSC method considered in this work was applied to the pre-processed EEG recordings using the ratio 30 : 90 and the parameters syntonization with the *Sparsest possible solution* like in the simulation experiments. So, for each subject and experimental condition, the dipole-wise source power was calculated and averaged in the time range from 227 to 383 *ms*, wich corresponds to the P300 component of ERP, as in [46]. Then, we compared the response to target stimuli between groups (ADHD vs. Control). Therefore, the potential difference of the power was evaluated between two cases: visual target ADHD group vs. visual target control group and auditory target ADHD group vs. auditory target control group. The comparison was carried out using a two-sided pairwise Student-t test. Significant differences in power were assumed for brain areas achieving t-scores with absolute values greater than 2.0639, corresponding to alpha levels $p < 0.05$, uncorrected.

3.3.6 Localization of emotion-related brain activity

The second real EEG data used in this study was obtained from the publicly available dataset for emotion analysis using physiological signals (DEAP) [47]. Thirty-two healthy participants (50% females and 50% males aging in average 26.9 years) who agreed to participate in the study were recorded using thirty-two-channel EEG data was recorded using a BIOSEMI Active Two system.

All participants were presented with forty one-minute long music videos with varying emotional content. Before every video, there was a baseline period of five seconds so that each participant was asked to concentrate at a cross in the middle of the screen. Following the presentation of each video, the participants were asked to rate the music videos on a discrete 9-point scale for valence, arousal, dominance, and liking. Valence, arousal, and dominance dimensions were scored using the self-assessment manikins (SAM) to gauge user emotional states [48]. The liking rate was used to inquire about the subject's tastes and not their feeling per se, and relied on a 9-point scale placed under thumbs down/up symbols.

Data were acquired at a 512 *Hz* sampling rate, placing the electrodes according to the international 10-20 system. Pre-processing included the following steps: common referencing, down sampling to 128 *Hz*, high-pass filtering from 4 *Hz*, and eye blink artifact removal using independent component analysis.

Source localization and statistical analysis: The DSC method considered in this work was applied to the pre-processed EEG recordings using the ratio 30 : 90 and the parameters syntonization with the *Sparsest possible solution* like in the simulation experiments. Later, the subject's subjective scores were thresholded at the mid-point of the 9-points scale, i.e., at 5, in order to configure low and high classes for each emotion. An illustration of the classes is depicted in Fig. **3-3**. Afterward, We computed the dipole-wise source power from the estimated brain activity of all the recordings available on the DEAP database. More-

over, taking as reference the thresholded scores, we compared two conditions for each subject and emotion, namely: Valence (negative-positive), Arousal (passive-active), Dominance (dominated-dominant), and Liking (dislike-like). The comparison was carried out using a two-sided pairwise Student-t test. Significant differences in power were assumed for brain areas achieving t-scores with absolute values greater than 2.0244, corresponding to alpha levels $p < 0.05$, uncorrected.

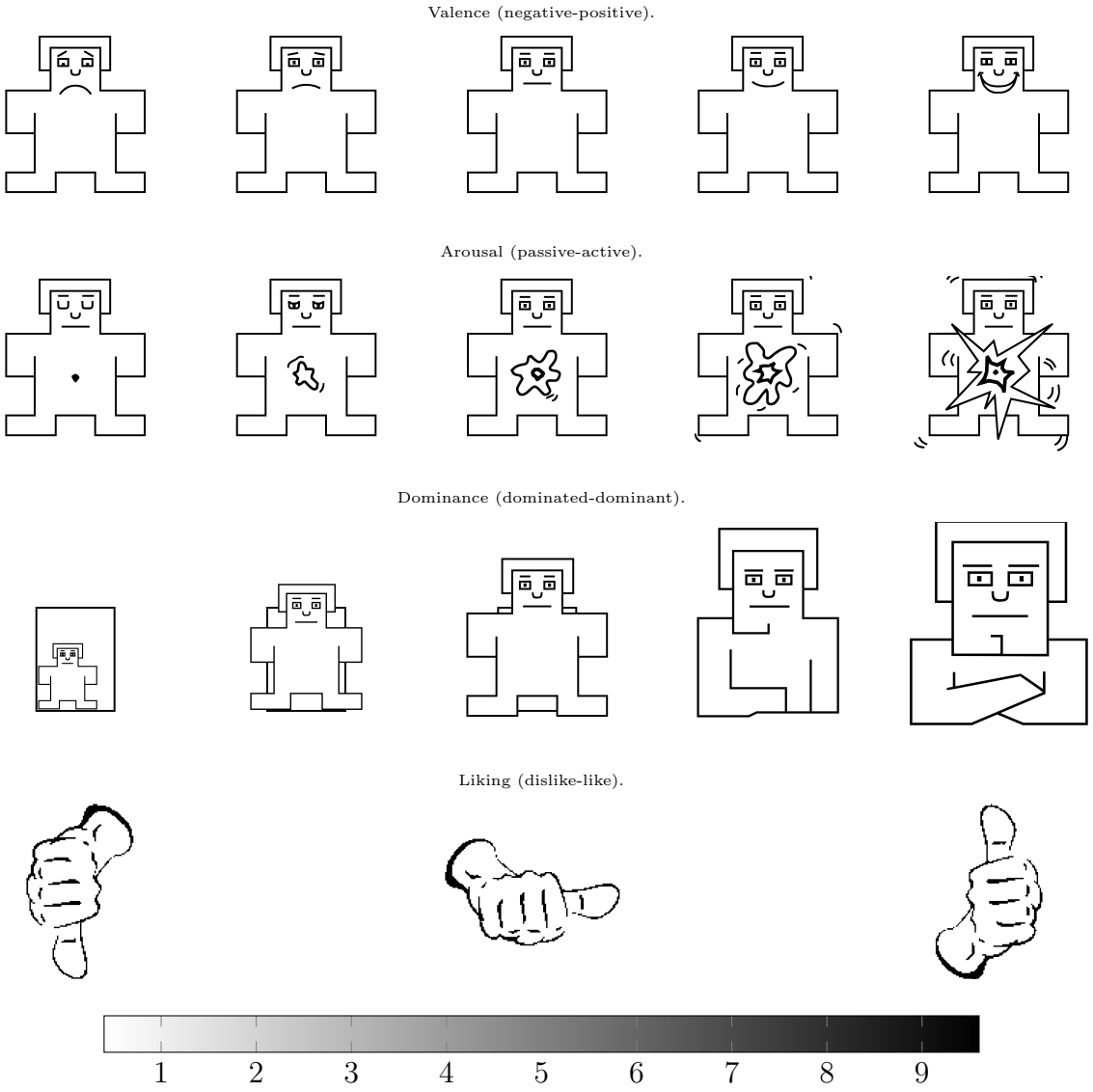

Figure **3-3**: The Self-assessment manikins scales $[1, 9]$ for the levels of valence, arousal, and dominance; and the thumbs down/thumbs up symbols for the liking scale $[1, 9]$

3.4 Results

3.4.1 Simulated data

The spatial and temporal reconstruction performance of DSC with several ratios and the two strategies for syntonization, S-FLEX, and MSP, on ERP simulated data is depicted in Figs. **3-4** and **3-6** for DSC with *Sparsest possible solution* and in Figs. **3-5** and **3-7** for DSC with *Residual norm criterion*. We observe that DSC(Lasso) and DSC(90:30) yield the lowest spatial accuracy (higher ε_s values) for all the number of active sources and SNR values. In contrast, DSC(90:90) and DSC(30:90) yield better spatial accuracy, which increase as the number of active sources becomes greater. These results make clear that the non-stationary temporal dynamics of the simulated EEG recordings clearly affect the performance of the proposed algorithms. Nevertheless, when only the temporal dynamics are considered, as in DSC(Fusion), the spatial accuracy decrease significantly. Results behave the same across all the tested SNR values. Finally, as expected, S-FLEX and MSP yield high spatial performance when temporal dynamics are soft (one active source), and decrease as the non-stationary activity augment. We observe a similar behavior regarding the temporal accuracy. In this case, as expected, methods that do not include temporal information, as DSC(Lasso), S-FLEX and MSP achieve the lowest temporal accuracies. Nevertheless, when only temporal constraints are included, as in DSC(Fusion), the temporal performance is low. Consequently, methods encouraging a compromise between spatial and temporal resolution, as DSC(90:30), DSC(90:90) and DSC(30:90) yield the higher average maximal correlation. This behavior on the spatial and temporal performance is extended to the epilepsy simulated data, which results are depicted in Figs. **3-8** and **3-10** for DSC with the *Sparsest possible solution* and in Figs. **3-9** and **3-11** for DSC with the *Residual norm criterion*
Summarizing, In both experiments *SD-1* and *SD-2* the DSC has similar behavior with the two tuning methods, however, it is preferable the *Sparsest possible solution* for though it is more heuristic has lower computational cost. In both tuning methods adjusting the spatial-to-temporal regularization ratio $\lambda_s : \lambda_t$, DSC can be tuned to emphasize either the spatial or temporal reconstruction, depending on the requirements for the specific data in hand.

3.4.2 Visual and auditory evoked potentials-related brain activity

Fig. **3-12** shows the sensor-space data, as well as the results of the source reconstruction using DSC with ratio 30 : 90 and syntonization strategy the *sparsest possible solution*, for the visual (Figs. 3.12(a) to 3.12(d)) and auditory (Figs. 3.12(e) to 3.12(h)) evoked potentials elicited by the target stimuli for representative subjects. Likewise, Fig. **3-13** shows the corresponding results for the non target stimuli. In the first subfigures ((a),(e)), the trial-wise stimulus-locked EEG time series are shown, the red vertical lines at 227 *ms* and 383 *ms*. In the second ((b),(f)), time series of the reconstructed activity. In the third subfigures ((c),(g)) the average scalp topography from 227 *ms* to 383 *ms*. The last subfigure ((d),(h))

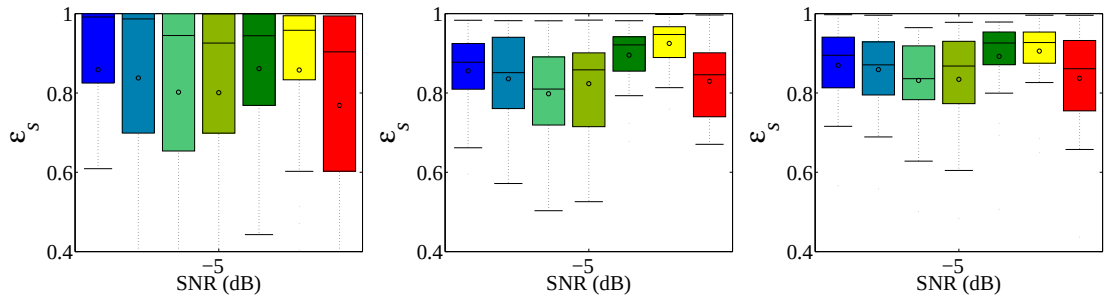

(a) One active source. (b) Three active sources. (c) Five active sources.

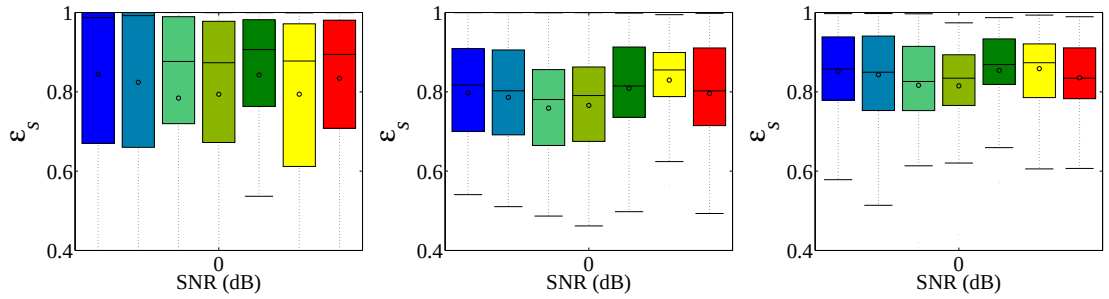

(d) One active source. (e) Three active sources. (f) Five active sources.

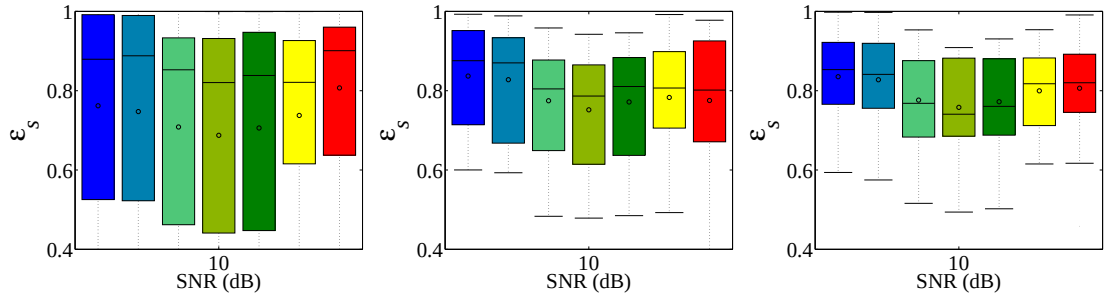

(g) One active source. (h) Three active sources. (i) Five active sources.

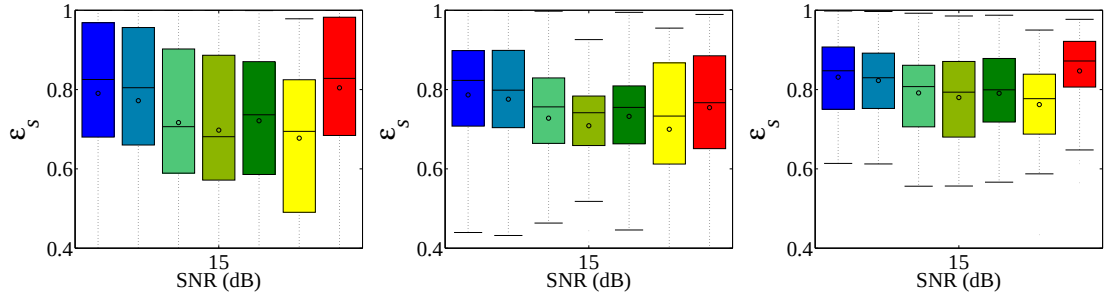

(j) One active source. (k) Three active sources. (l) Five active sources.

Figure **3-4**: Spatial reconstruction accuracy according to ε_s in *SD-1* for the following mappings methods: DSC(Lasso) DSC(90 : 30) DSC(90 : 90) DSC(30 : 90) DSC(Fusion) S-FLEX MSP. The DSC uses the *Sparsest possible solution*

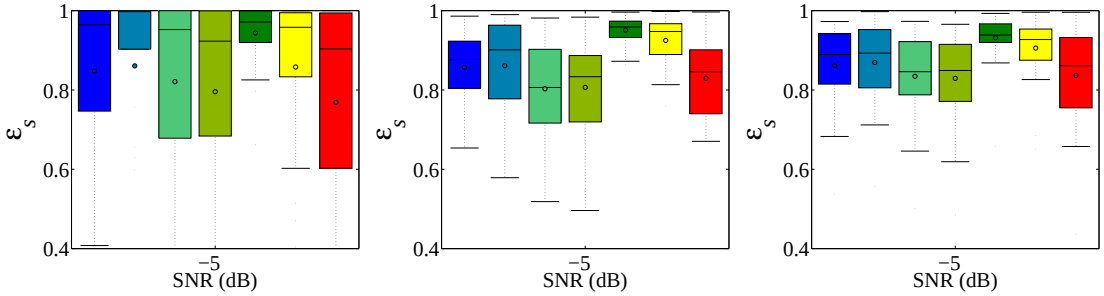

(a) One active source. (b) Three active sources. (c) Five active sources.

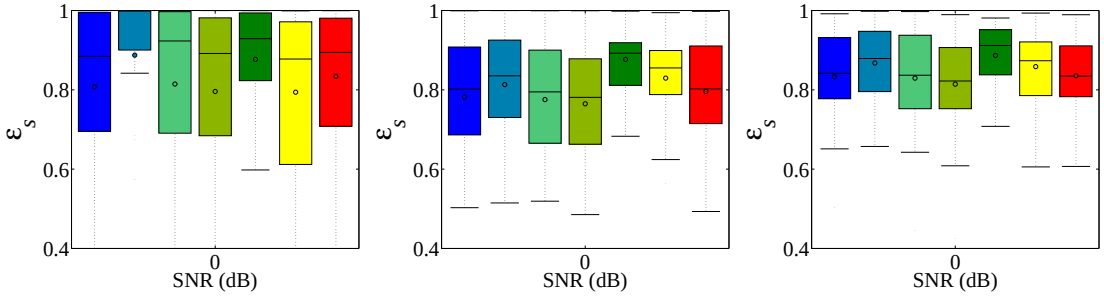

(d) One active source. (e) Three active sources. (f) Five active sources.

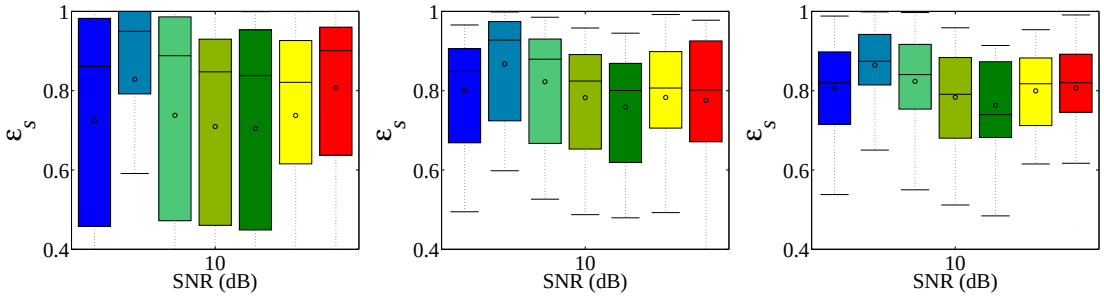

(g) One active source. (h) Three active sources. (i) Five active sources.

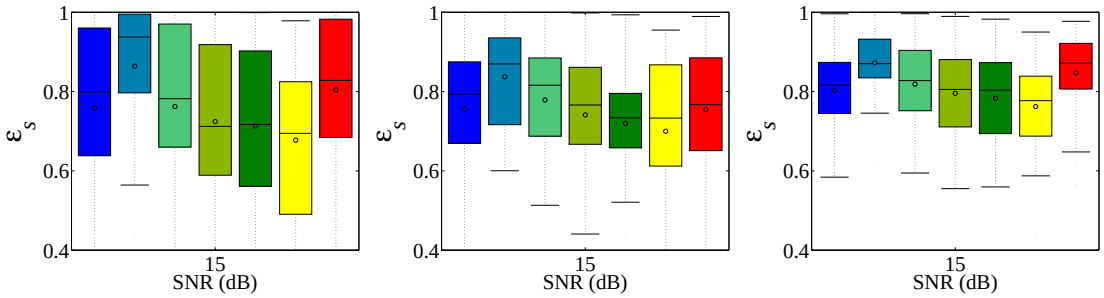

(j) One active source. (k) Three active sources. (l) Five active sources.

Figure **3-5**: Spatial reconstruction accuracy according to ε_s in *SD-1* for the following mappings methods: DSC(Lasso) DSC(90 : 30) DSC(90 : 90) DSC(30 : 90) DSC(Fusion) S-FLEX MSP. The DSC uses the *Residual norm criterion*

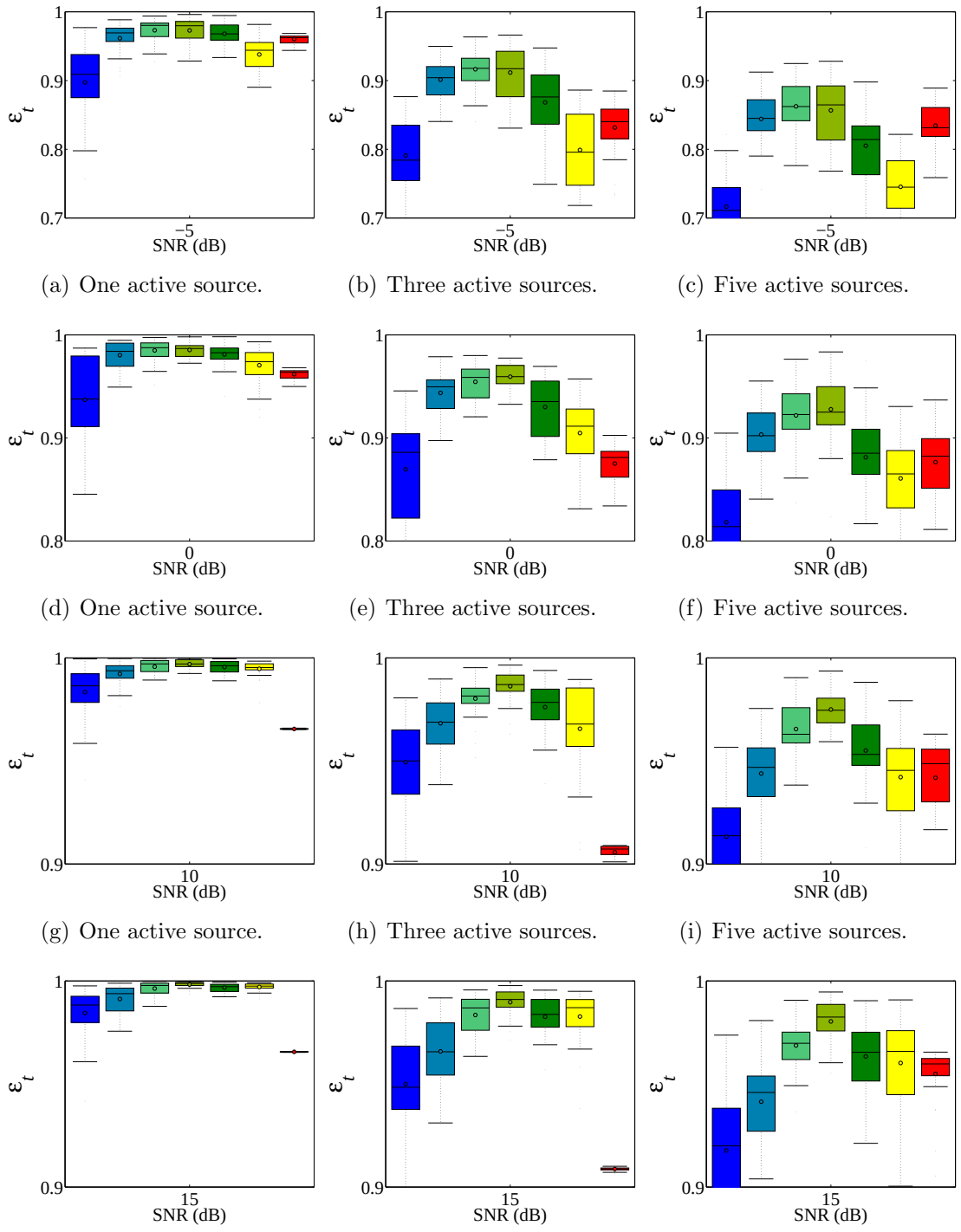

(a) One active source. (b) Three active sources. (c) Five active sources.

(d) One active source. (e) Three active sources. (f) Five active sources.

(g) One active source. (h) Three active sources. (i) Five active sources.

(j) One active source. (k) Three active sources. (l) Five active sources.

Figure **3-6**: Temporal reconstruction accuracy according to ε_t in *SD-1* for the following mappings methods: DSC(Lasso) DSC(90 : 30) DSC(90 : 90) DSC(30 : 90) DSC(Fusion) S-FLEX MSP. The DSC uses the *Sparsest possible solution*

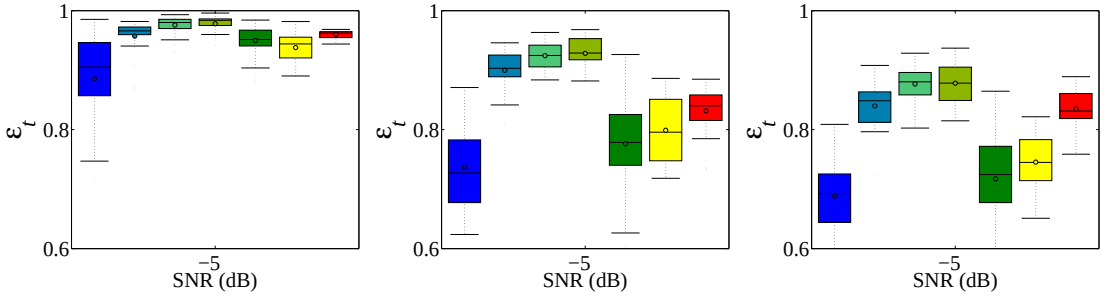

(a) One active source. (b) Three active sources. (c) Five active sources.

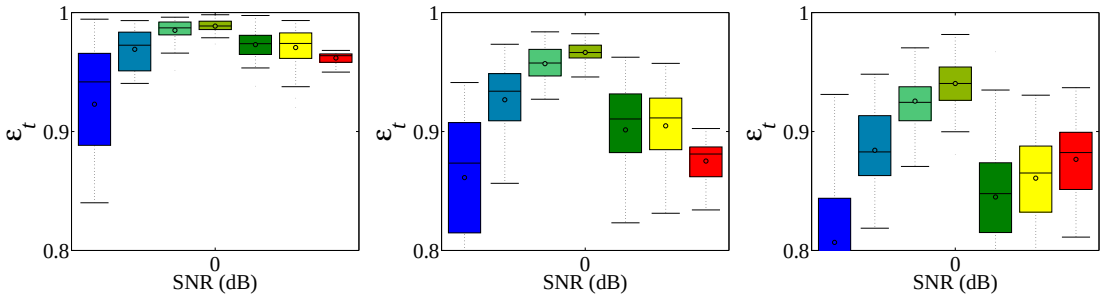

(d) One active source. (e) Three active sources. (f) Five active sources.

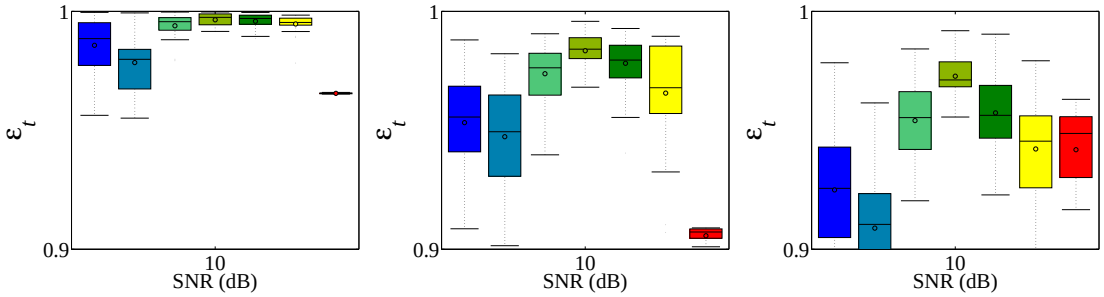

(g) One active source. (h) Three active sources. (i) Five active sources.

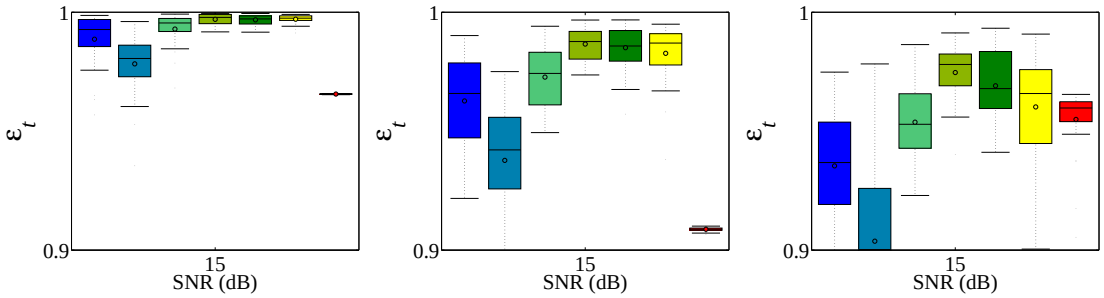

(j) One active source. (k) Three active sources. (l) Five active sources.

Figure **3-7**: Temporal reconstruction accuracy according to ε_t in *SD-1* for the following mappings methods: DSC(Lasso) DSC(90 : 30) DSC(90 : 90) DSC(30 : 90) DSC(Fusion) S-FLEX MSP. The DSC uses the *Residual norm criterion*

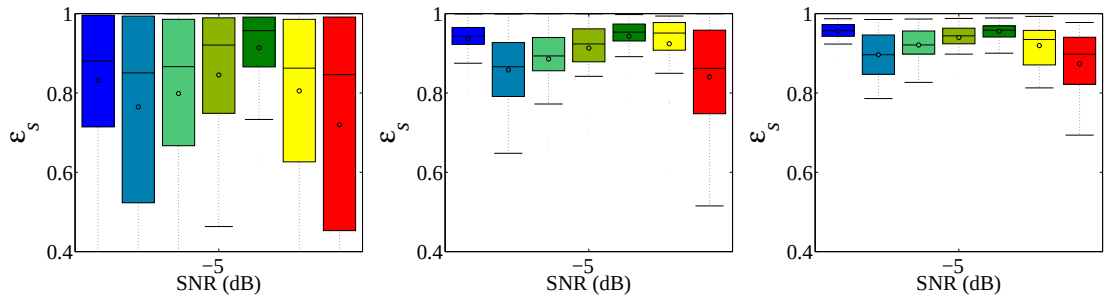

(a) One active source. (b) Three active sources. (c) Five active sources.

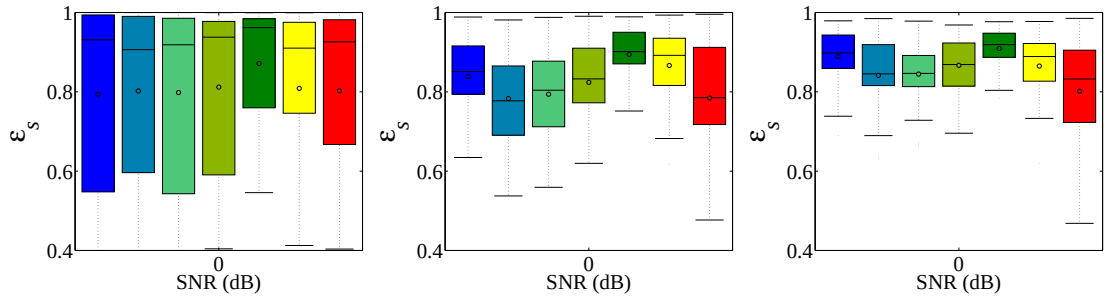

(d) One active source. (e) Three active sources. (f) Five active sources.

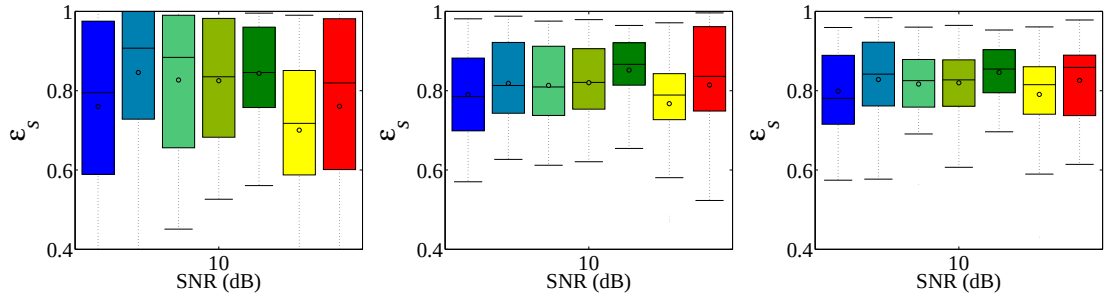

(g) One active source. (h) Three active sources. (i) Five active sources.

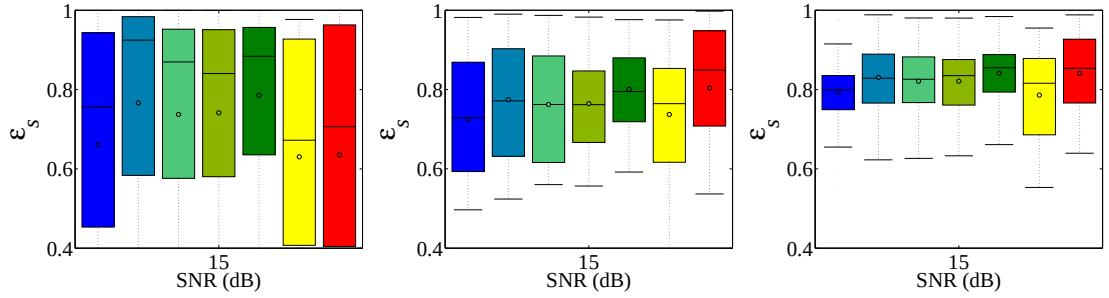

(j) One active source. (k) Three active sources. (l) Five active sources.

Figure **3-8**: Spatial reconstruction accuracy according to ε_s in *SD-2* for the following mappings methods: DSC(Lasso) DSC(90 : 30) DSC(90 : 90) DSC(30 : 90) DSC(Fusion) S-FLEX MSP. The DSC uses the *Sparsest possible solution*

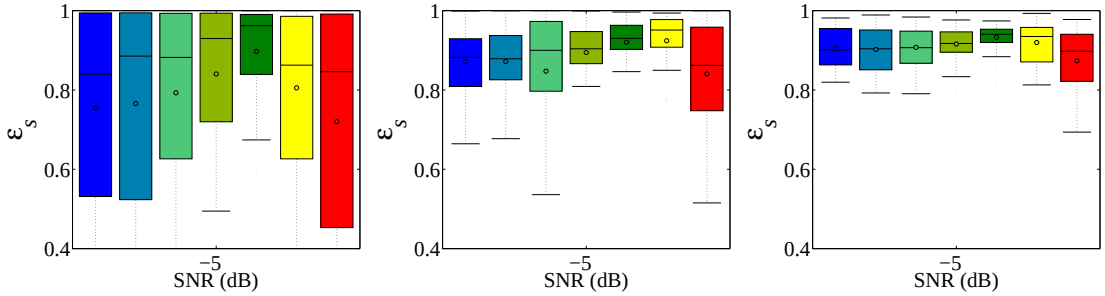

(a) One active source. (b) Three active sources. (c) Five active sources.

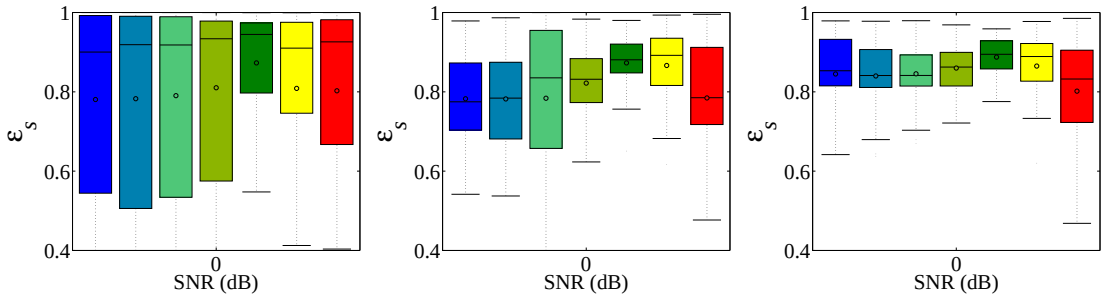

(d) One active source. (e) Three active sources. (f) Five active sources.

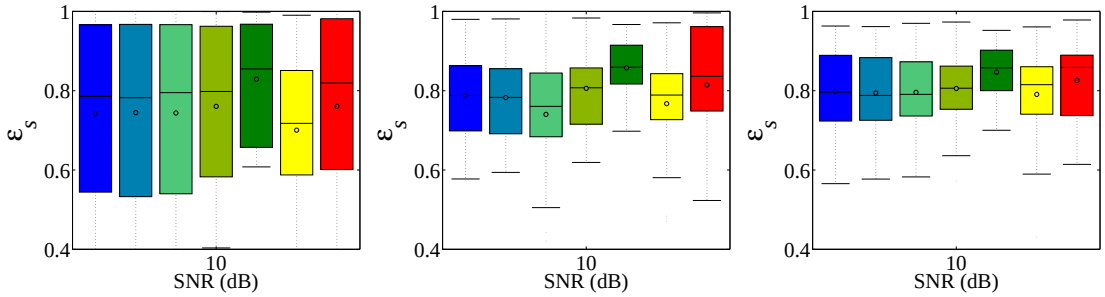

(g) One active source. (h) Three active sources. (i) Five active sources.

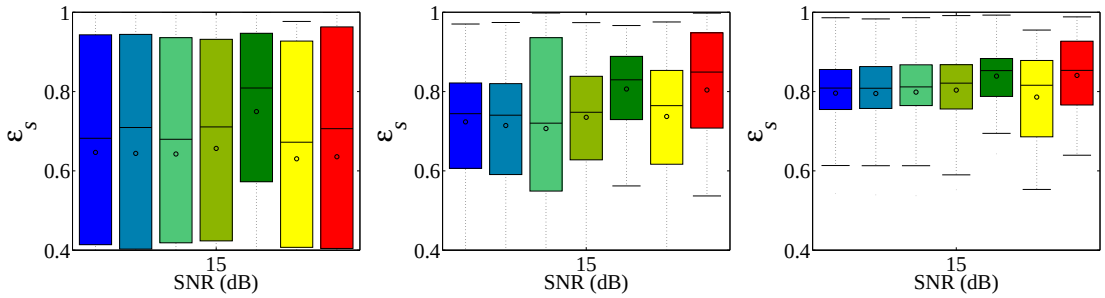

(j) One active source. (k) Three active sources. (l) Five active sources.

Figure **3-9**: Spatial reconstruction accuracy according to ε_s in *SD-2* for the following mappings methods: DSC(Lasso) DSC(90 : 30) DSC(90 : 90) DSC(30 : 90) DSC(Fusion) S-FLEX MSP. The DSC uses the *Residual norm criterion*

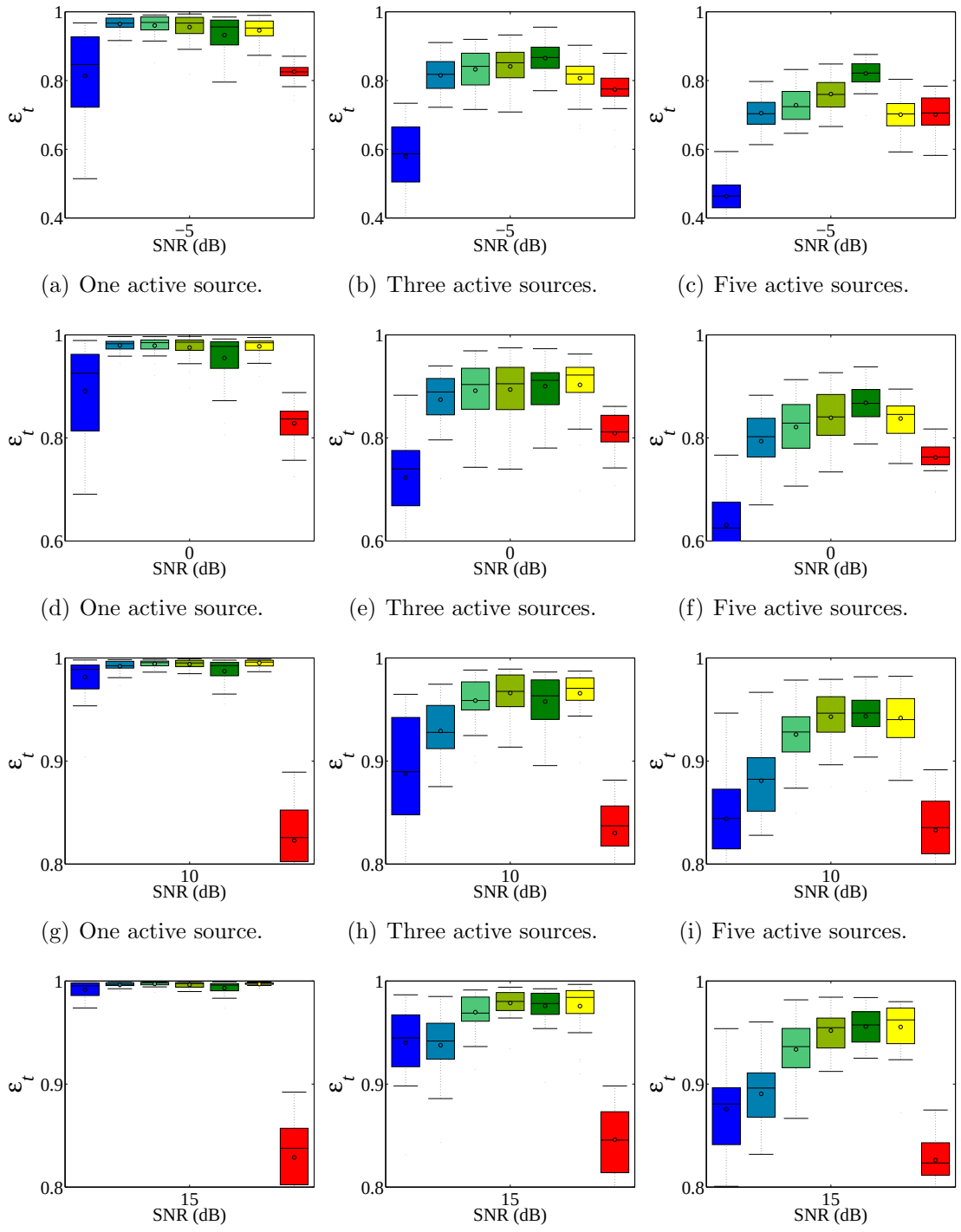

(a) One active source. (b) Three active sources. (c) Five active sources.

(d) One active source. (e) Three active sources. (f) Five active sources.

(g) One active source. (h) Three active sources. (i) Five active sources.

(j) One active source. (k) Three active sources. (l) Five active sources.

Figure **3-10**: Temporal reconstruction accuracy according to ε_t in *SD-2* for the following mappings methods: DSC(Lasso) DSC(90 : 30) DSC(90 : 90) DSC(30 : 90) DSC(Fusion) S-FLEX MSP. The DSC uses the *Sparsest possible solution*

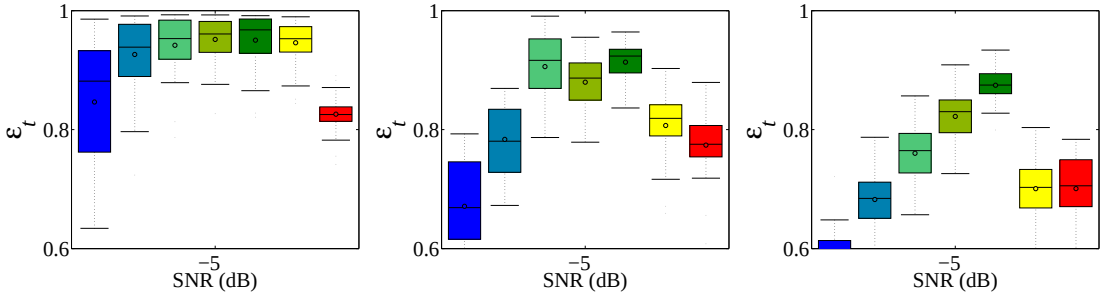

(a) One active source. (b) Three active sources. (c) Five active sources.

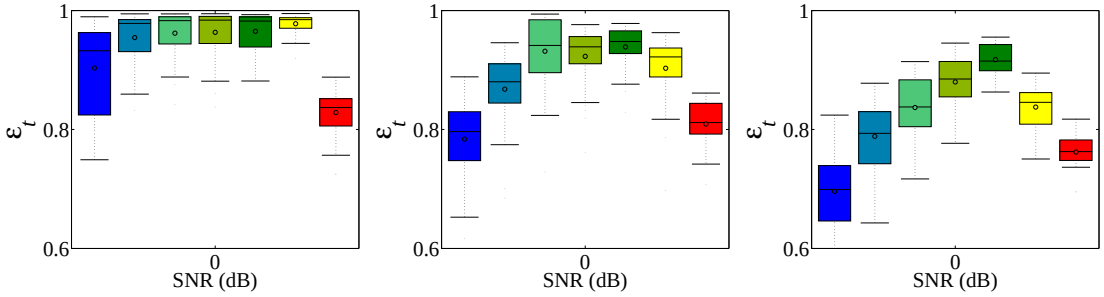

(d) One active source. (e) Three active sources. (f) Five active sources.

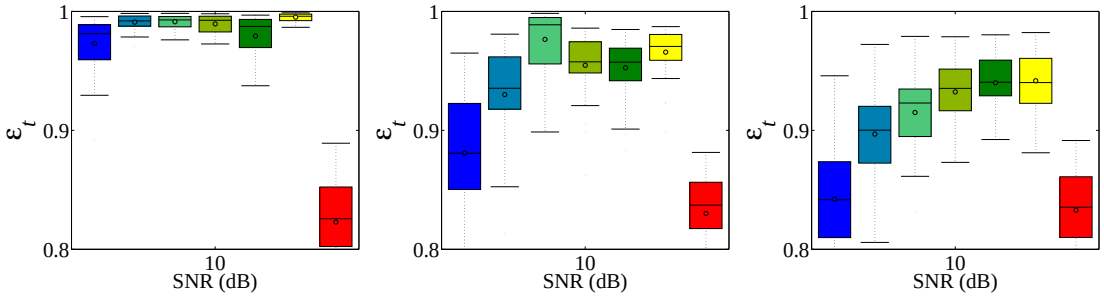

(g) One active source. (h) Three active sources. (i) Five active sources.

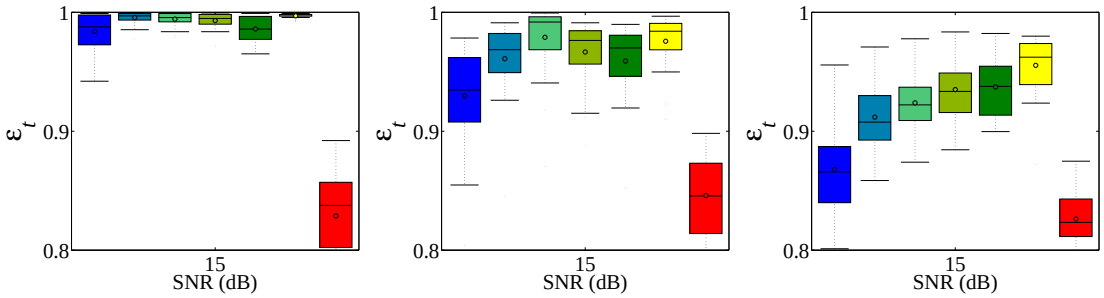

(j) One active source. (k) Three active sources. (l) Five active sources.

Figure **3-11**: Temporal reconstruction accuracy according to ε_t in *SD-2* for the following mappings methods: DSC(Lasso) DSC(90 : 30) DSC(90 : 90) DSC(30 : 90) DSC(Fusion) S-FLEX MSP. The DSC uses the *Residual norm criterion*

shows the corresponding source reconstruction in the same time range. The time range 227 ms to 383 ms was selected for presentation, since it corresponds to the P300 component of ERP [46]. For both visual and auditory stimulation, DSC localizes components of the P300 in the prefrontal cortex coinciding with studies which suggest that deficits or dysregulation in subregions of the prefrontal cortex may carry to the spectrum of ADHD symptoms [49, 50, 51] as follows: the dorsolateral prefrontal cortex regulates attention, and its impairment may lead to symptoms of inattention and distraction, the right inferior prefrontal cortex regulates behavior, and its impairment may carry to symptoms of impulsivity and hyperactivity, and finally, the ventromedial prefrontal cortex regulates emotions responses. Particularly, in the case of visual stimulation is seen actives areas in the neighborhood of the occipital cortex, which it is consistent with stimulation produced. In the case of auditory stimulation there are actives zones near the superior parietal lobule associated to functions related to the memory like the working memory and visuospatial memory which coincides with types of ADHD and its association with spatial working memory deficits [52], also there are minimum actives areas in the temporal lobe associated with the stimulus. In all cases, the reconstructed time series draws a clean representation of the dynamics found in the original ERP responses, and the cortical reconstruction shows actives areas proximate to the actives zones in the scalp map. Generally, we observe that target stimuli lead to more local regions of estimated brain activity, while non-target stimuli the activity seems to be more dispersed.

Source localization and statistical analysis: Fig. **3-14** shows the results of dipole-wise Student-t test for differences in power between groups (ADHD vs. Control) for visual and auditory target stimuli respectively. Here, dark blue color denotes higher activity in the condition mentioned first, while dark red color denotes higher activity in the condition mentioned second. In both cases, significant differences (red areas of higher intensity) were found in brain areas nearby attention networks ventral and dorsal. This is consistent with studies that have found reduced activity in these attention networks in children with ADHD, like in [53, 54, 55]. Particularly, with the visual stimuli there are active areas by the posterior cingulate gyrus that has associated functions with the memory like topographic and topokinetic memory, and functions with the high-demand visual processing, and by the posterior inferior temporal gyrus associated with the visual fixation and sustained attention to color and shape. For the auditory stimuli, we found actives areas in the gyrus rectus involve in auditory non-speech processing, the temporal pole that response to auditory stimulation, and in the middle temporal gyrus relate to processing complex sounds. Also, it is noted that in both conditions of stimulation, the significant differences are given only to positive values. This means that the amplitude of the activity related to P300 has a greater amplitude in control subjects than in subjects ADHD. In both stimuli, these differences are seen in the network of frontoparietal attention. The results are consistent with recent studies that show in this network reductions in the amplitude of P300 in areas surrounding this region in children with ADHD.

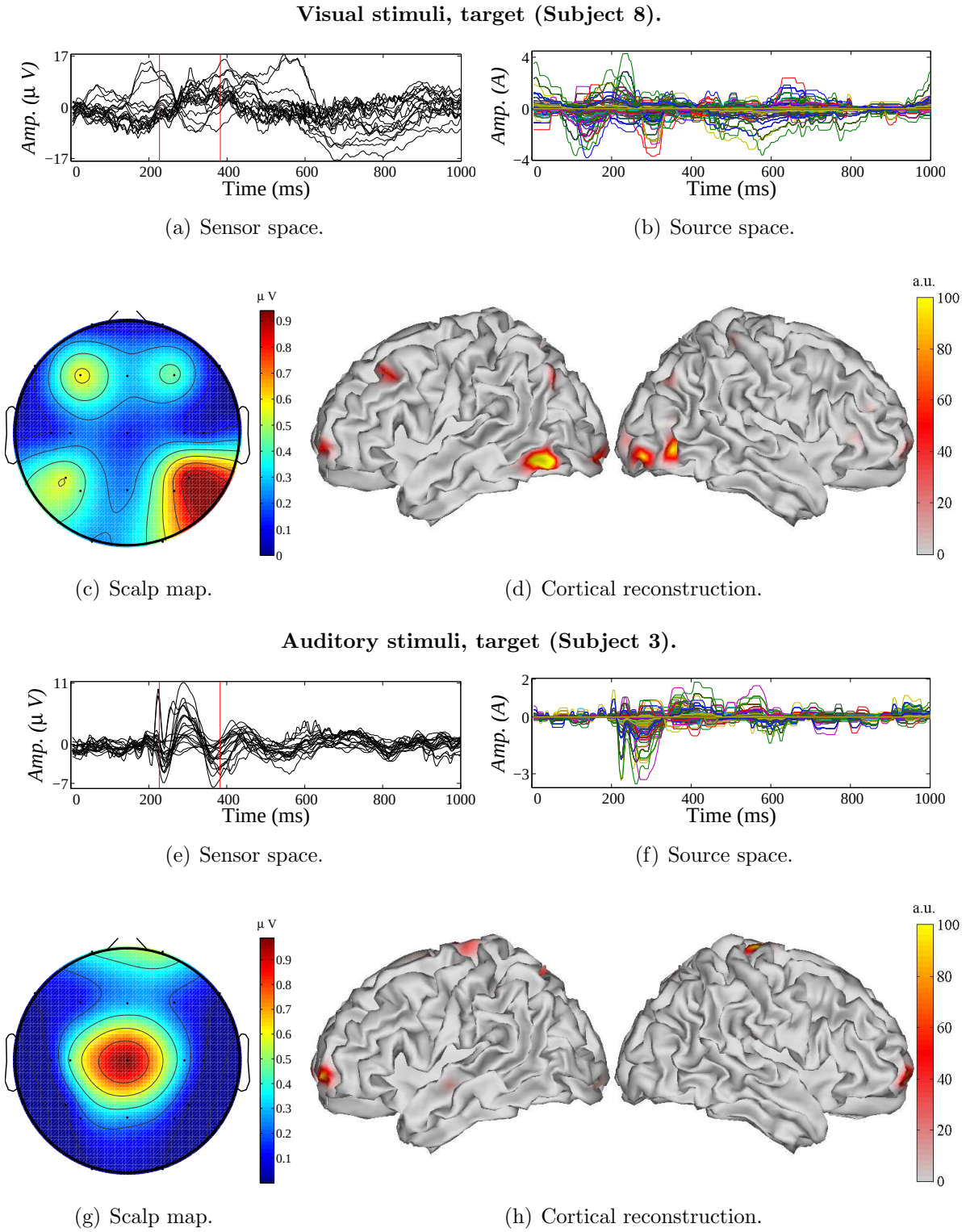

(a) Sensor space. (b) Source space.

(c) Scalp map. (d) Cortical reconstruction.

(e) Sensor space. (f) Source space.

(g) Scalp map. (h) Cortical reconstruction.

Figure **3-12**: Sensor-space EEG data and DSC source reconstruction of visual and auditory evoked potentials elicited by *target* stimuli for representative subjects.

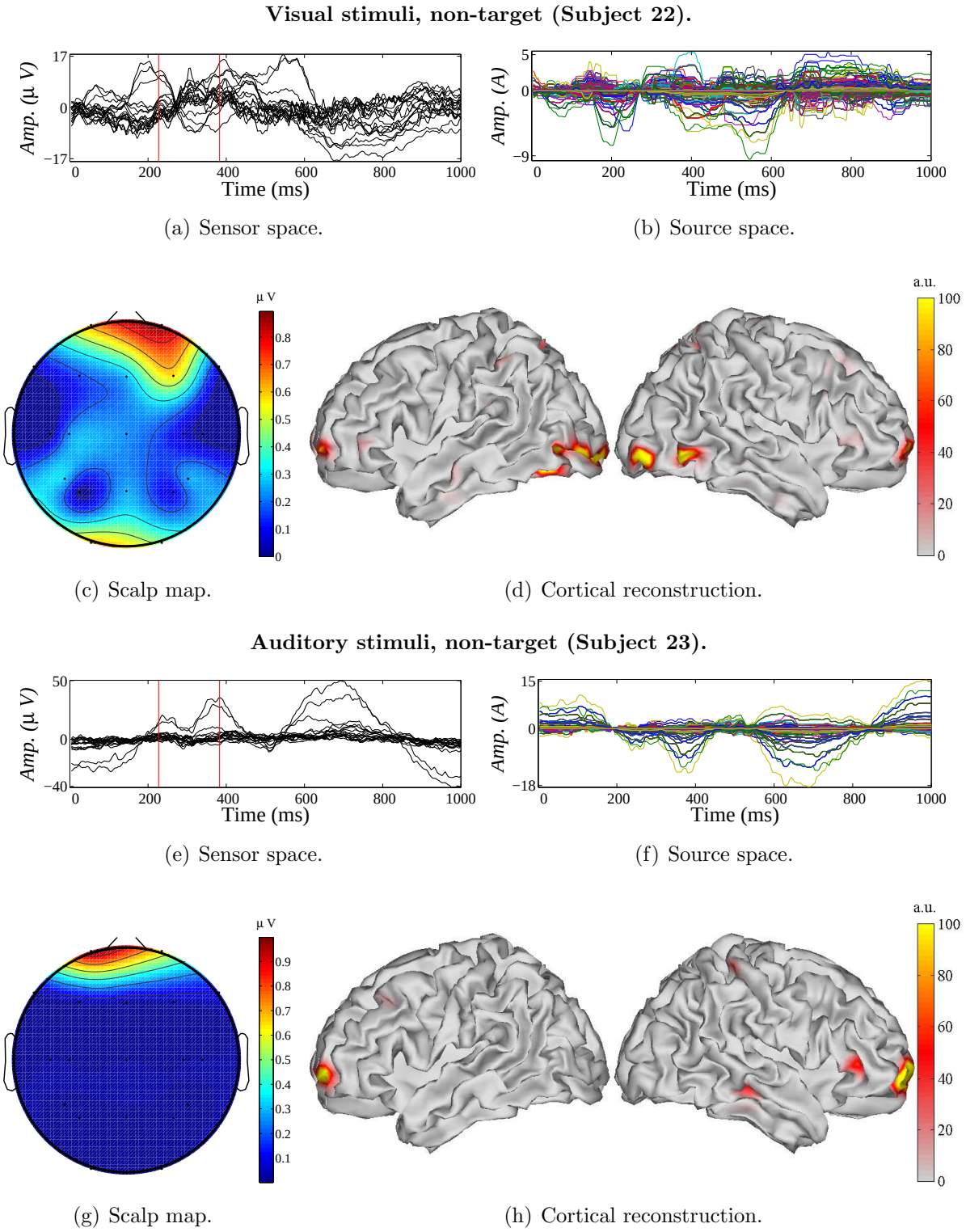

(a) Sensor space.

(b) Source space.

(c) Scalp map.

(d) Cortical reconstruction.

(e) Sensor space.

(f) Source space.

(g) Scalp map.

(h) Cortical reconstruction.

Figure **3-13**: Sensor-space EEG data and DSC source reconstruction of visual and auditory evoked potentials elicited by *non-target* stimuli for representative subjects.

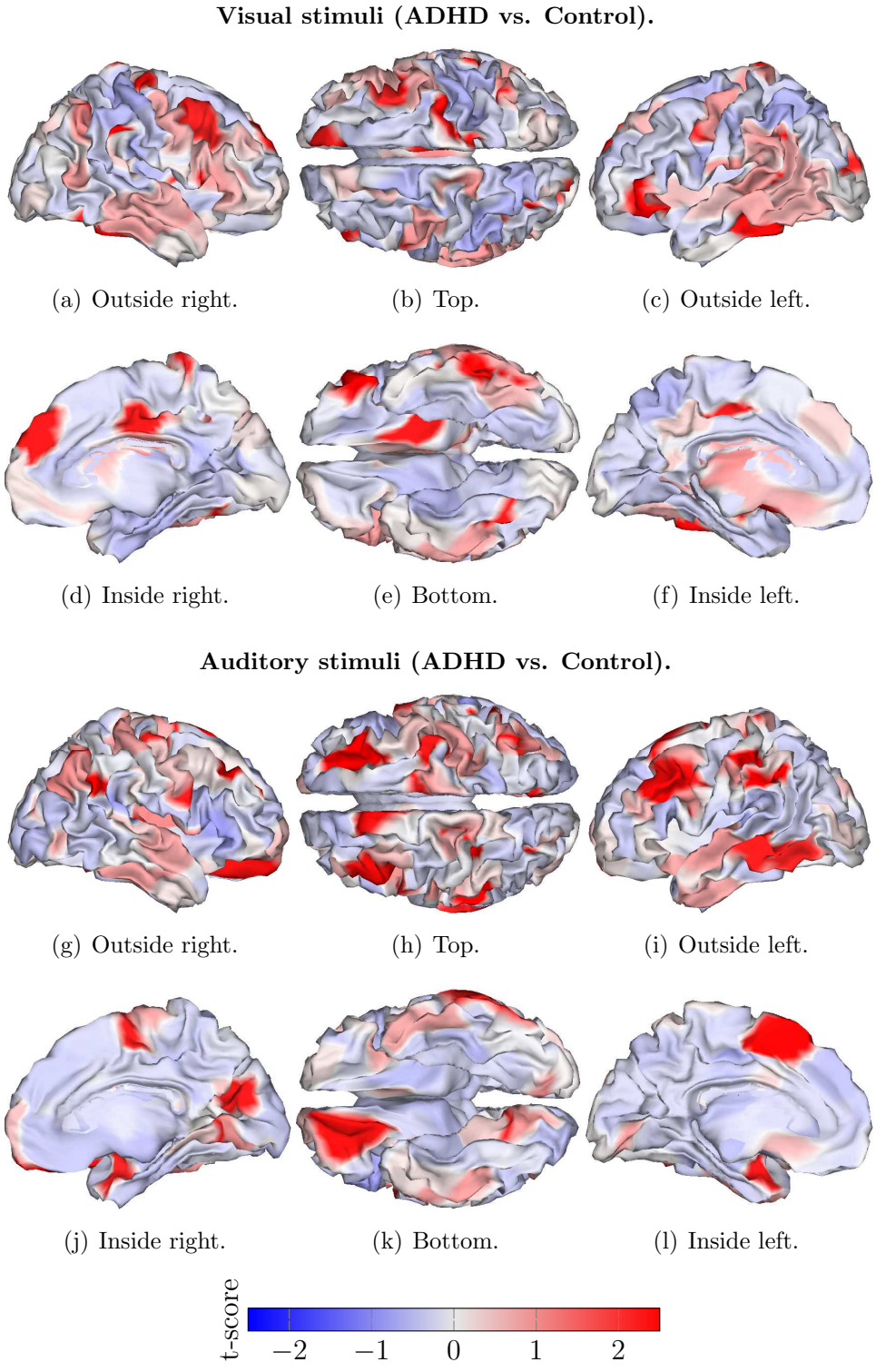

Figure **3-14**: Differences in source power estimated by DSC for ERPs analysis with visual and auditory stimuli between groups (ADHD vs. Control).

3.4.3 Emotion-related brain activity

Source localization and statistical analysis: Figs. **3-15** and **3-16** show examples of the dipole wise Student-t test results for differences in power between classes, namely, high/low valence, high/low arousal, high/low dominance, high/low liking, respectively. Dark blue color denotes higher activity in the low classes, while dark red color denoted higher activity in the high classes. Results were obtained using DSC(30:90) and syntonization strategy the *sparsest possible solution* as it was the source reconstruction algorithm that achieved better results with simulated data. However, in the next chapter, a comparison of all the tested methods for the emotion-based database is carried out.

For valence emotion, cerebral regions showing statistically significant differences (darker blue and red areas) are found near to the default-mode network. For positive valence (darker red), differences were found in the medial frontal and prefrontal cortex associated with pleasant and unpleasant emotions, and the posterior cingulate gyrus area involved in emotions, indeed, there is a close association between emotion/motivation and memory. Whereas for negative valence (darker blue), differences were found in the inferior parietal lobule region related to the retrieval of unpleasant experiences, the somatosensory cortex and the frontal eye field related to processing emotions. For arousal, regions showing significant differences were observed mainly for active activity (higher arousal rates). For instance, there is a high active area near to the ventral anterior cingulate gyrus area, which is related to the sexual arousal to visual stimuli in males, also, the temporal pole related with visual processing of emotional images, and the gyrus rectus related to emotional components of behavior are active. For passive activity (lower arousal rates) significant differences were found in the posterior cingulate gyrus associated with the process of semantic emotional information and the action of passively listening to different sentences, similarly, several areas related to visual stimuli processing were found active during this kind of activity like the middle occipital gyrus that response to emotions.

When the subject felt dominant (high dominance values), the superior parietal lobule, related to processing emotions and self-reflections during decision making, shows high activity. Also, the posterior cingulate gyrus, related to fear conditioning and evaluative judgment shows significant differences. And when the subject felt dominated (low dominance values) part of the prefrontal cortex related to pleasant and unpleasant emotions and the attribution of intention of others shows high activity. Finally, for liking, regions related to evaluative judgment, as the posterior cingulate gyrus were found active when the subject dislike the video, likewise, the inferior parietal lobule associated with retrieval of unpleasant experiences was active. In contrast, areas as the inferior frontal gyrus, which is related to music enjoyment was found active when the subject liked the video.

Finally, for all emotions, an active brain area around the secondary visual cortex was found. This is expected because this area is highly related with response to emotion/attention in visual processing.

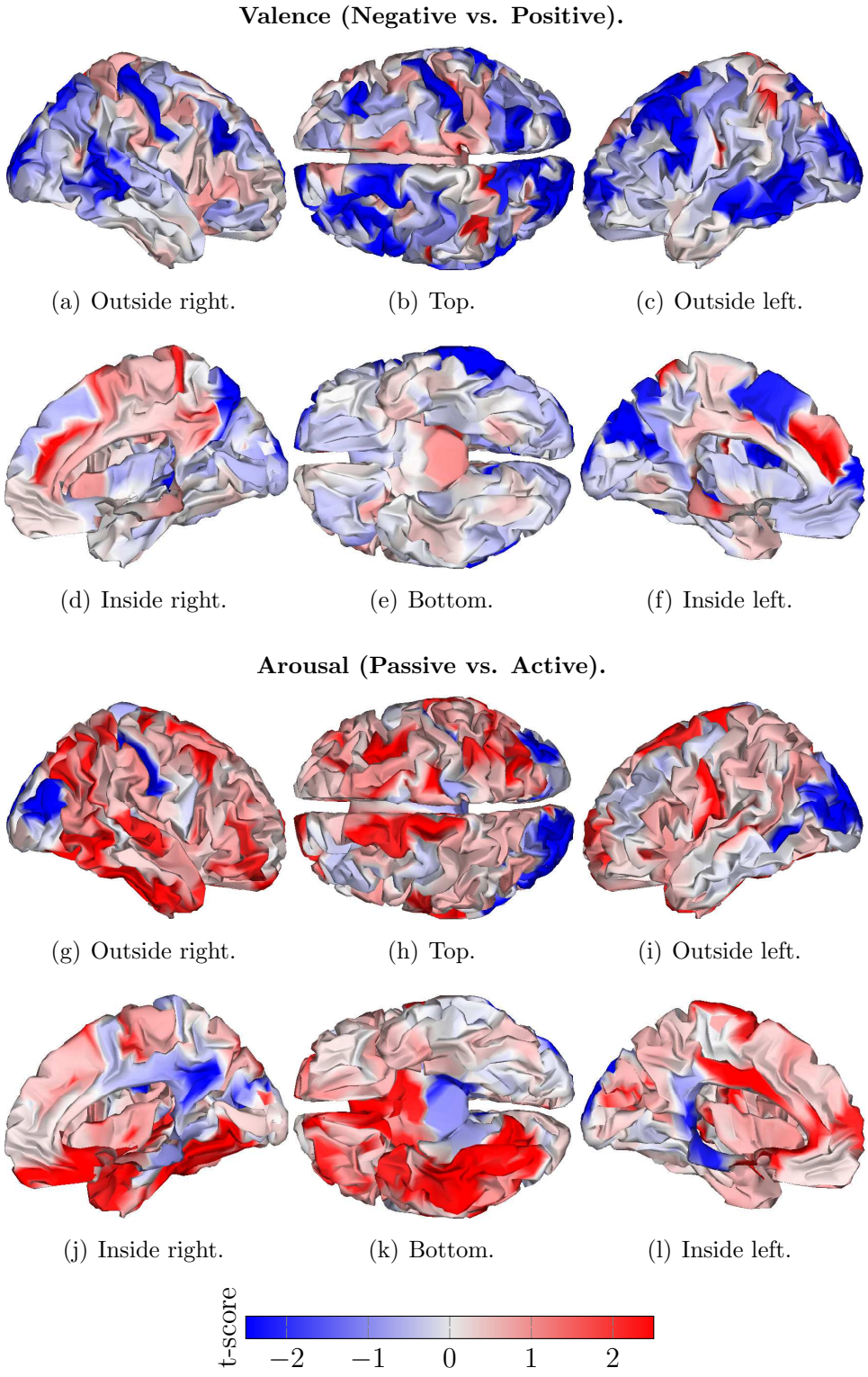

Figure **3-15**: Differences in source power estimated by DSC for Valence (Negative vs. Positive) subject 12 and for Arousal (Passive vs. Active) subject 29.

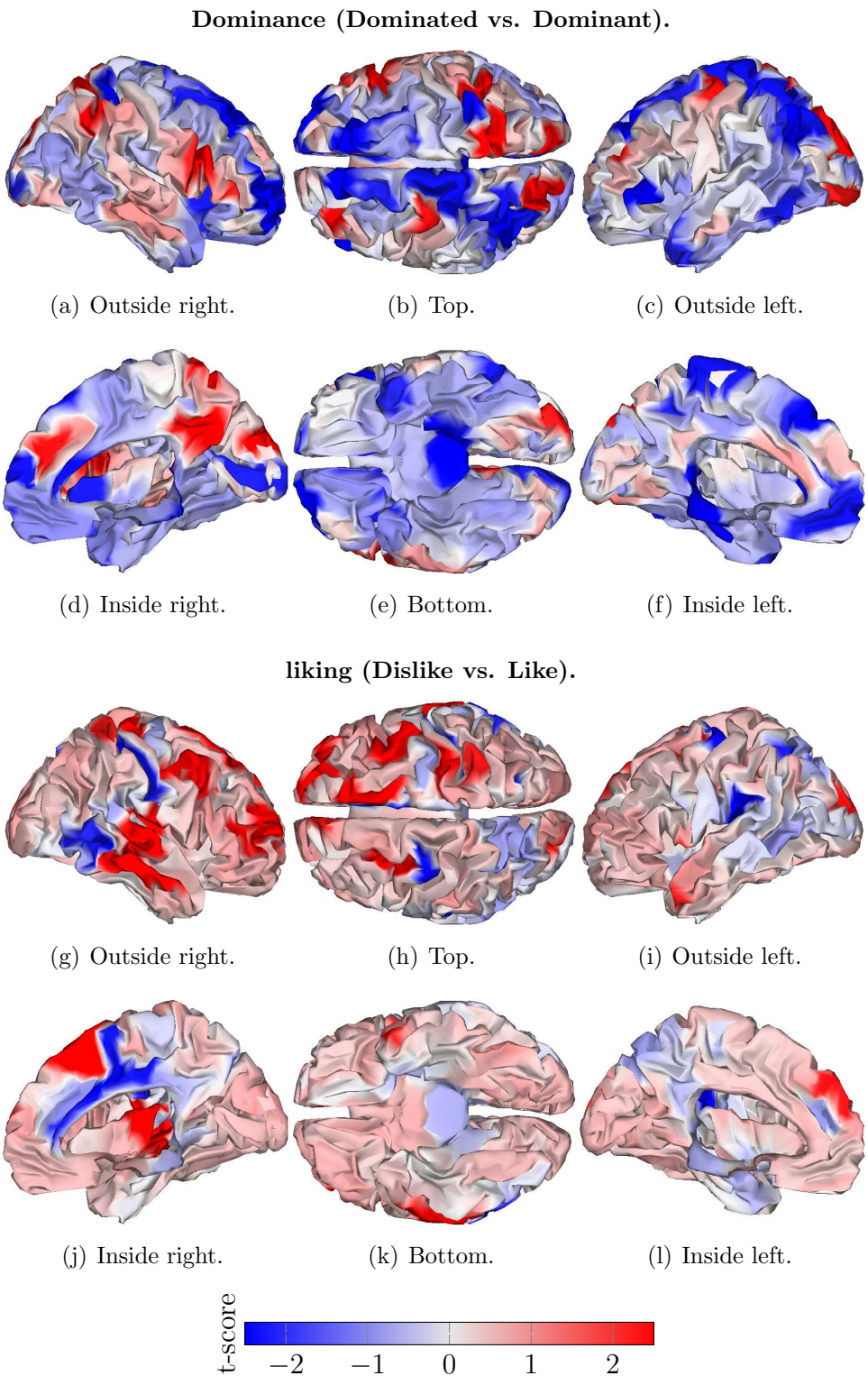

Figure **3-16**: Differences in source power estimated by DSC for Dominance (Dominated vs. Dominant) subject 15 and for Liking (Dislike vs. Like) subject 20.

3.5 Discussion

In this chapter, we proposed a regularized method for neural activity reconstruction that explicitly included both (space and time) constraints on the solution of the M/EEG inverse problem. The main goal is to reach a suitable trade-off between the corresponding space and time resolutions, aiming to improve the estimation of the active sources with powerful non-stationary brain activity. By the above-obtained results, the following findings are worth mentioning.

We fostered the enhancement of the spatial resolution by representing the brain activity as the sum of a small number of space basis functions, describing smooth localized patches of potentially active brain regions [12, 11, 39]. Additionally, we incorporated a spatial constraint expressed in terms of the L_1-norm. This norm fostered the solution to be sparse, making the estimated brain activity be represented mainly by the concentrated sources. Besides, the influence of the spatial constraint on the estimated solution was ruled by increasing or decreasing the regularization parameter λ_s. Furthermore, we included a temporal regularization term that encourages the inverse problem solution to improve the temporal accuracy of the accomplished neural activity reconstruction. This term that penalizes the difference between consecutive time points yields a smooth solution over time.

We expected that in the asymptotic cases ($\lambda_s = 0$, or $\lambda_t = 0$), the spatial or temporal resolution of our DSC based approach would achieve the better results, respectively. Nevertheless, we were surprised that the behavior was completely opposite, i.e, in both asymptotic cases we found the worst results. However, we achieved outstanding results when a proper compromise between both regularization parameters was defined. As a result, we found that depending on the dynamic of the data in hand; we could set a proper regularization ratio between the spatial and temporal parameter to enhance the performance of our DSC based approach.

One of the most crucial stages for DSC to achieve a good performance is the syntonization of the regularization parameters. In this regard, we have used two different strategies, namely, the *Sparsest possible solution*, and the *Residual norm criterion*. Although the later strategy may achieve better results, it is necessary to compute several solutions with different parameters, which is an exhaustive search, and it demands high computational cost just for one recording. On the other hand, we have shown empirically that the *Sparsest possible solution* also achieves a good performance, and it does not demand an exhaustive computational cost. Consequently, we recommend this approach as a good alternative for tuning the regularization parameters.

4 Source connectivity analysis to emotion classification

4.1 Introduction

In the previous chapter, we have proposed an approach to solve the M/EEG inverse problem. Several approaches to solve the M/EEG inverse problem in order to localize and reconstruct sources of brain activity by taking advantage of the spatiotemporal properties of brain dynamics. Nevertheless, in the last decades, neuroimaging techniques have also been widely used to identify brain networks involved in normal brain functions [22, 23], as well as in neurological disorders such as epilepsy, autism, among others [28, 56], and even in analyzing how those networks behave in emotional states [57, 58].

As a first approach, connectivity measures have been applied to the sensor level recordings. Nevertheless, their interpretation is not straightforward as these recordings suffer from a low spatial resolution and are severely corrupted by effects of field spread [59]. One promising alternative to cope with these issues is the M/EEG source connectivity analysis that quantifies the activity interactions between distant brain areas. Connectivity source analysis comprises three main steps: *i*) Source estimation from scalp M/EEG measurements, *ii*) Identification of Regions of Interest (ROIs) and their respective time courses, and *iii*) Assessment of the connectivity between pairs of ROIs, measuring the interactions between separated brain areas. In this regard, it is expected that the final result, i.e., the identified networks, will directly depend on the chosen methods in each step. Consequently, the choice of the best combination of methods is crucial to reveal the actual networks that are active during a considered brain process.

In this chapter, we show how our DSC based brain mapping method could be easily extended as a source connectivity approach. To this end, we take advantage of the spatial basis used to reconstruct the brain activity to define the ROIs describing brain areas with compact neighboring regions. In this regard, the estimated time courses of each spatial basis will correspond to the time course of each ROI. Finally, the *Magnitude Square Coherence (MSC)* is computed between pairs of ROIs to determine their connectivity.

We validate the proposed approach of source connectivity analysis for discriminating emotional states, where the results are promising, making the proposed methodology a suitable alternative to support many neurophysiological applications.

4.2 Methods

The proposed methodology for source connectivity assessment using spatiotemporal constraints involves these three stages: *i*) Identification of regions of interest (ROIs), *ii*) Estimation of ROI time courses from the scalp M/EEG measurements, and *iii*) Assessment of the pairwise connectivity between all selected ROIs.

4.2.1 ROI identification

As a rule, M/EEG source connectivity analysis demands an accurate identification of the ROI set, because the quality of the estimation of their time courses is a critical issue to describe the information flow inside the brain [22]. Here, we solve this problem by setting each column of the spatial basis set $\boldsymbol{\Phi}$, defined in Eq. (3-3) as an individual ROI. In this way, the set of ROIs are designed to cover the entire cortical surface, and each ROI is described by a compact neighboring region.

4.2.2 Estimation of ROI time courses

In order to assess the connectivity between pairs of distant brain regions, M/EEG recordings $\boldsymbol{Y}$ must be evaluated in the source space $\boldsymbol{J}$, i.e., the scalp neural field data should be projected through the lead field matrix $\boldsymbol{L}$ into the brain volume by solving an inverse problem (see Eq. (3-1)). Additionally, given that the quality of connectivity analysis is very influenced by the adequate extraction of the ROI time courses, the temporal non-stationarity inherent to brain activity must be carefully considered. Here, we solve both problems by estimating the brain activity inside predefined spatial patches (ROIs), using the DSC based approach, as follows:

$$\widehat{\boldsymbol{H}} = \underset{\boldsymbol{H}}{\operatorname{argmin}}\{||\boldsymbol{Y} - \boldsymbol{L}\boldsymbol{\Phi}\boldsymbol{H}||_F^2 + \lambda_s||\boldsymbol{H}||_1 + \lambda_t \sum_{t\in T-1} ||\boldsymbol{h}_{t+1} - \boldsymbol{h}_t||_1\}, \tag{4-1}$$

Consequently, each row vector $\boldsymbol{h}_r \in \mathbb{R}^T, \forall r = 1 : R$ of the matrix $\boldsymbol{H}$ holds the time course of its corresponding ROI, and their estimation holds the spatiotemporal dynamics of brain activity, as explained above.

4.2.3 Assessment of functional connectivity between pairs of ROIs

To assess the connectivity between each pair of ROIs, we use the *Magnitude Square Coherence* (MSC) that is a large-scale measure of the underlying dynamic neural interactions, where higher coherence values indicate greater functional interplay between the two underlying neural networks [58]. Consequently, the pair-wise MSC between two ROIs r and r' can be computed as [60]:

$$\gamma_{\boldsymbol{h}_r,\boldsymbol{h}_{r'}}(f) = \frac{|S_{\boldsymbol{h}_r\boldsymbol{h}_{r'}}(f)|^2}{S_{\boldsymbol{h}_r\boldsymbol{h}_r}(f)S_{\boldsymbol{h}_{r'}\boldsymbol{h}_{r'}}(f)},\ \gamma_{\boldsymbol{h}_r,\boldsymbol{h}_{r'}}(f) \in \mathbb{R}^+ \tag{4-2}$$

where $\boldsymbol{h}_r \in \mathbb{R}^T$ is the r-th ROI time course, $S_{\boldsymbol{h}_r \boldsymbol{h}_{r'}}(f) \in \mathbb{R}^+$ is the cross-spectral density between ROIs r and r' at the frequency f, and $S_{\boldsymbol{h}_r \boldsymbol{h}_r}(f) \in \mathbb{R}^+$ and $S_{\boldsymbol{h}_{r'} \boldsymbol{h}_r}(f) \in \mathbb{R}^+$ are the auto-spectral density of $\boldsymbol{h}_r$ and $\boldsymbol{h}_{r'}$, respectively. Moreover, to quantify the dependencies, the averaged MSC, $\overline{\gamma}_{\boldsymbol{h}_r, \boldsymbol{h}_{r'}} \in \mathbb{R}^+$, is computed over a predefined frequency rank $f \in [f_1, f_2]$.

4.3 Experiments

4.3.1 Source connectivity analysis to emotion classification

Here, we use the proposed source connectivity analysis method as a feature extraction approach to classify emotional states. We use the EEG data described in the previous chapter for emotion analysis using physiological signals (DEAP). Consequently, obtained connections are used to solve four different binary classification problems, namely low/high valence, low/high arousal, low/high dominance, low/high liking. The proposed source connectivity analysis approach to classify emotional states is depicted in Fig. 4-1.

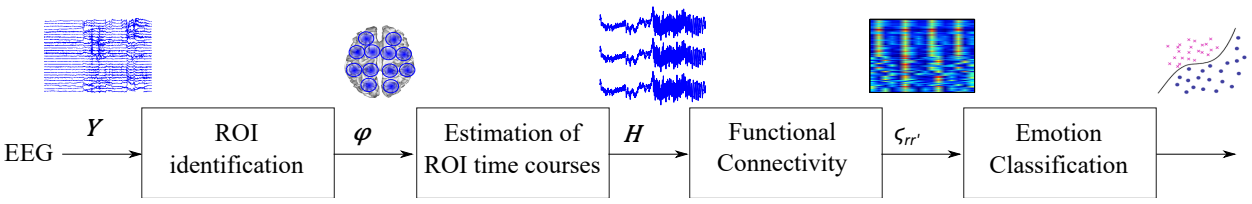

Figure **4-1**: Illustration of the proposed source connectivity analysis steps.

Estimation of ROIs: We selected the ROIs as each element of the spatial basis $\boldsymbol{\Phi}$. Consequently, the associated time course to each ROI corresponds to the row vectors of matrix $\boldsymbol{H}$ denoted as $\boldsymbol{h}_r \in \mathbb{R}^{1 \times T}, \forall r = 1 : 512$. This procedure holds for our DSC based approach and for S-FLEX. To MSP, all dipoles belonging to each element of the spatial basis were averaged in order to obtain a single time course representing the ROI temporal structure. Finally, to avoid biased connectivity estimation between ROIs that are not actually active, and for computing the same number of features than for the sensor space based connectivity, we selected the $R' = 32$ most powerful ROIs.

Estimation on connectivity between pairs of ROIs: Once the set of ROIs is selected, we proceeded to estimate their connections using the *Magnitude Squared Coherence (MSC)* metric that allows to quantify linear synchrony in different frequency bands, as MSC has been shown to be associated with information regarding emotions [58]. The MSC was applied to each possible pair of ROIs (and pairs of channels for the comparing sensor based approach) by splitting the 1-minute time courses into thirty 2-second long epochs without overlap. The obtained MSC values were averaged over epochs to get a more trustworthy metric. Before

computing the MSC metric, to obtain a holistic view of the information transfer using this linear metric MSC was calculated for the frequency range $4-45\,Hz$, comprising information of the theta ($\theta = 4-8Hz$), alpha ($\alpha = 8-12Hz$), beta ($\beta = 12-30Hz$), and gamma ($\gamma = 30-45Hz$) frequency bands. As a result, a connectivity matrix $\mathbf{\Gamma}\in[0,1]^{R\times R}$ was computed.

Finally, as the coherence is a measure that assumes linear relationships, meaning that the square matrix $\mathbf{\Gamma}$ becomes symmetric with ones on the main diagonal, only their upper diagonal values are contemplated to create the feature representation matrix $\boldsymbol{\Upsilon}\in\mathbb{R}^{N_{tr}\times Q}$ with the minimum possible redundant information. As a result, each row vector of $\boldsymbol{\Upsilon}$ comprises $Q = R'(R'-1)/2$ features, corresponding to the $R'(R'-1)/2$ connections over the studied frequency rank of interest.

Statistical analysis: Based on the ROI-wise source connectivity, we searched for networks presenting significant differences between two different conditions per emotion (low/high classes), using a two sided Student-t test, individually for each subject. Once again, significant differences were assumed for connections between ROIs featuring t-scores with absolute values greater than 2.0244 (alpha level $p < 0.05$, uncorrected).

Classification training and validation: Additionally, towards classifying various emotional dimensions, each participant's subjective ratings were used as the ground truth values, and high and low classes were created as explained above. Afterward, emotion classification is performed individually per subject, using the feature matrix $\boldsymbol{\Upsilon}$ to feed a soft-margin *Support Vector Machine (SVM)* classifier. This classifier was trained under the following leave-one-out cross-validation methodology: *i*) From the $N_{tr} = 40$ trials per subject, 39 were used to train the SVM classifier, while the remaining sample was left for testing, *ii*) Repeat the preceding stage until all samples have been used as a test sample. The reason for using a leave-one-out cross-validation scheme was that the number of samples per subject is not enough for generating significant training and testing sets. Furthermore, this strategy is the most used for emotion discrimination using the DEAP database [61].

Finally, as the imposed threshold used to configure the high/low classes generated unbalanced classes for each subjective rating, the F1 score was employed to describe reliably the results of classifier performance while tackling the class unbalance, as suggested in [58]. However, accuracy rates were also computed to compare against some state-of-art methods facing the same problem.

4.4 Results

Statistical analysis: Figs. 4-2 to 4-8 show networks presenting significant differences between high/low classes for all the tested source localization methods. We observe that for

valence, arousal, and dominance, all tested methods find several significant connections related to the brain areas that presented higher activity in the experiment explained above. For instance, in valence emotion, several connections between the secondary visual cortex and the default mode network were found. Furthermore, in arousal, several connections between the temporal pole and the ventral anterior cingulate area were drawn. For dominance, we found very interesting that connections were found mostly between parts of the same brain hemisphere, mainly between the secondary visual cortex and the prefrontal cortex, which is related to pleasant and unpleasant emotions. This prefrontal cortex was also connected with the superior parietal lobe. Finally, we were surprised that liking almost not presented significant connections.

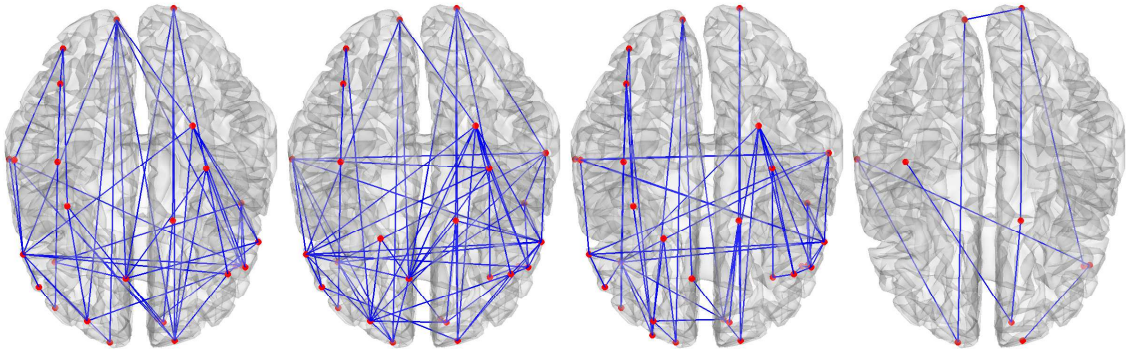

(a) Valence. (b) Arousal. (c) Dominance. (d) Liking.

Figure **4-2**: Source connectivity based on the DSC(Lasso) mapping

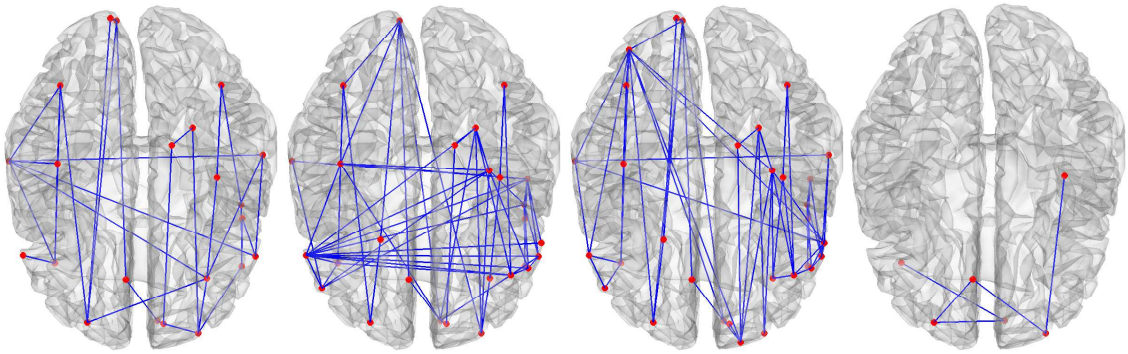

(a) Valence. (b) Arousal. (c) Dominance. (d) Liking.

Figure **4-3**: Source connectivity based on the DSC(90 : 30) mapping

Emotion classification: Finally, Table 4-1 reports the F1-score and classification accuracy averaged across subjects for the valence, arousal, dominance and liking categories. We ob-

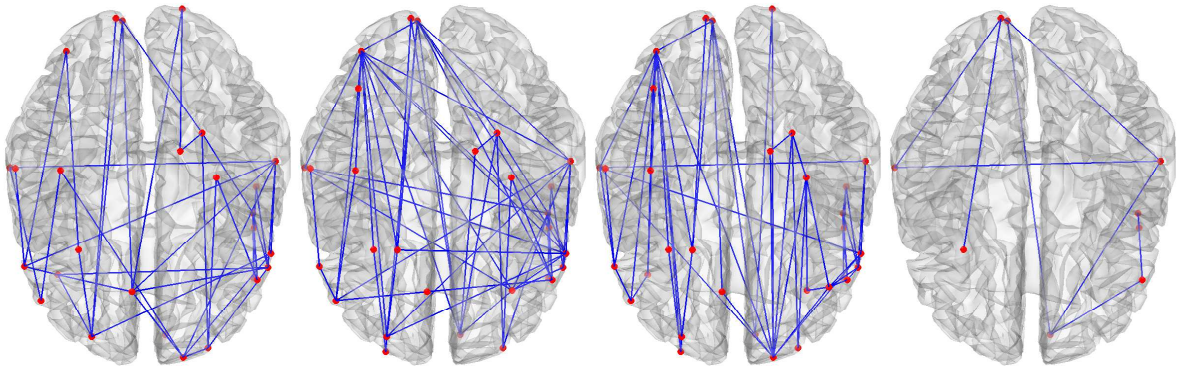

(a) Valence. (b) Arousal. (c) Dominance. (d) Liking.

Figure **4-4**: Source connectivity based on the DSC(90 : 90) mapping

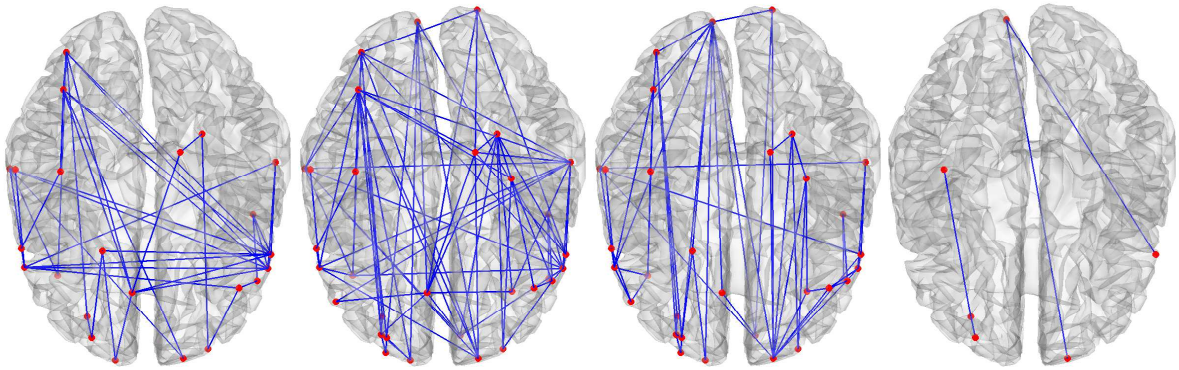

(a) Valence. (b) Arousal. (c) Dominance. (d) Liking.

Figure **4-5**: Source connectivity based on the DSC(30 : 90) mapping

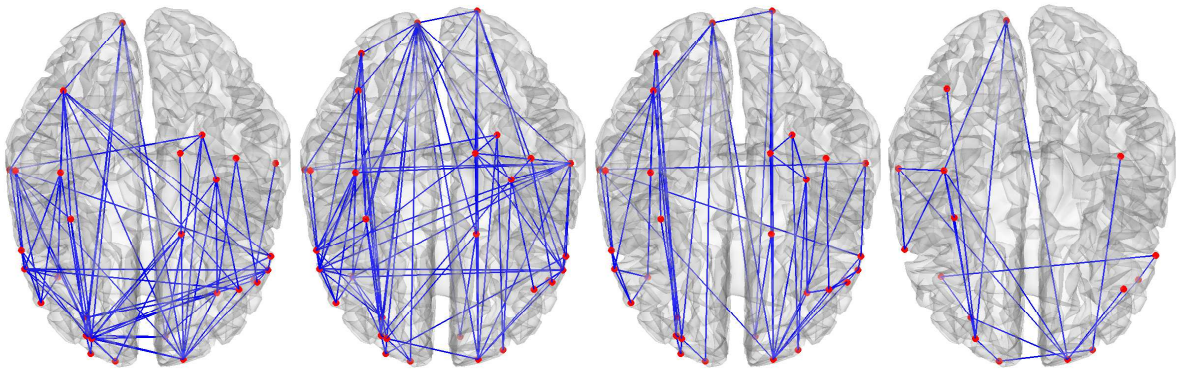

(a) Valence. (b) Arousal. (c) Dominance. (d) Liking.

Figure **4-6**: Source connectivity based on the DSC(Fusion) mapping

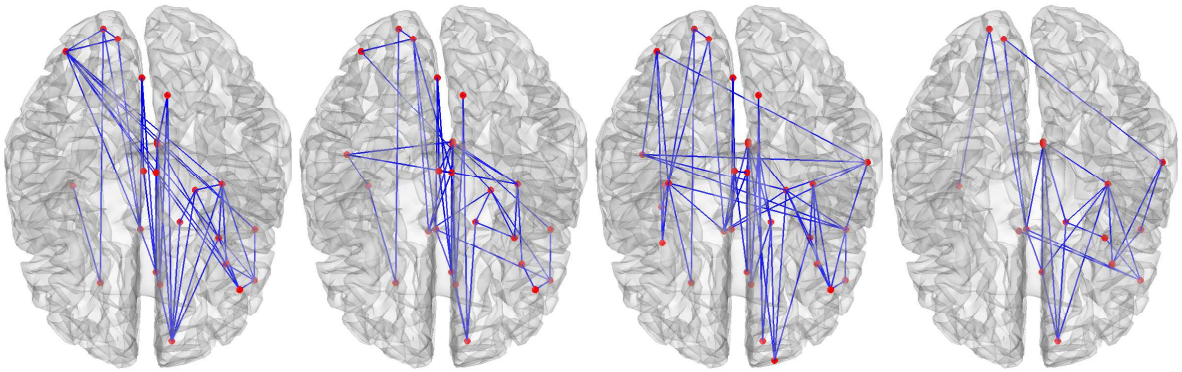

(a) Valence. (b) Arousal. (c) Dominance. (d) Liking.

Figure **4-7**: Source connectivity based on the S-FLEX mapping

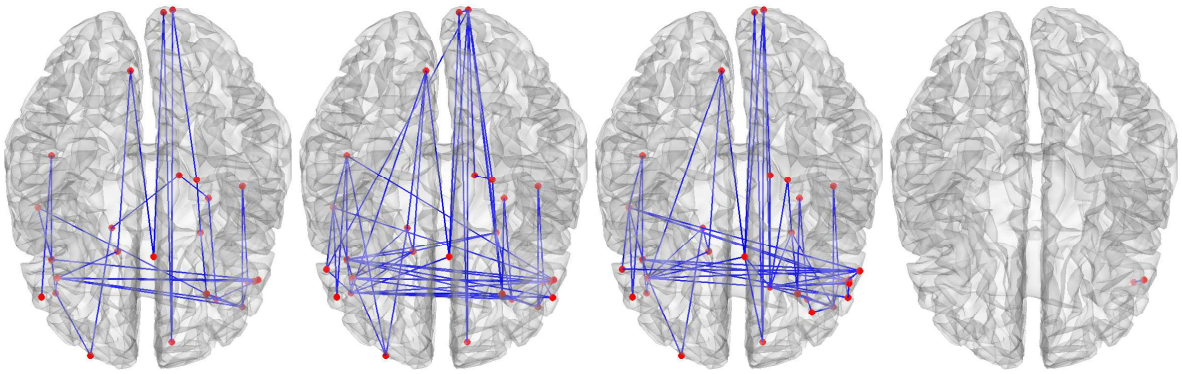

(a) Valence. (b) Arousal. (c) Dominance. (d) Liking.

Figure **4-8**: Source connectivity based on the MSP mapping

		EEG	**DSC**					**Sflex**	**MSP**
			Spa	90:30	90:90	30:90	**Tem**		
Ac	**V**	65.7 ± 10.9	63.7 ± 11.0	59.0 ± 10.5	63.6 ± 10.8	66.1 ± 10.1	65.2 ± 11.5	50.4 ± 15.9	58.1 ± 10.5
	A	53.5 ± 13.5	57.0 ± 11.8	58.0 ± 11.3	58.0 ± 13.1	56.0 ± 11.8	55.1 ± 12.8	54.3 ± 13.2	56.9 ± 12.9
	D	59.5 ± 11.5	60.2 ± 13.2	57.9 ± 12.3	60.2 ± 12.1	56.7 ± 15.1	56.0 ± 15.3	52.2 ± 14.1	55.3 ± 14.2
	L	59.0 ± 13.3	58.1 ± 14.7	59.0 ± 14.9	56.1 ± 18.7	58.0 ± 15.0	58.4 ± 16.0	55.4 ± 13.9	55.1 ± 13.0
F1	**V**	66.7 ± 11.9	64.2 ± 13.3	61.2 ± 9.7	65.5 ± 10.9	66.9 ± 12.1	65.7 ± 14.2	52.0 ± 19.0	59.6 ± 12.0
	A	55.3 ± 14.6	59.3 ± 14.2	61.3 ± 14.2	60.3 ± 15.4	57.7 ± 14.8	57.1 ± 14.6	52.8 ± 21.7	57.5 ± 15.9
	D	62.8 ± 11.3	63.8 ± 13.9	61.8 ± 13.3	64.3 ± 11.8	59.9 ± 15.0	58.4 ± 14.7	53.9 ± 19.0	57.7 ± 16.7
	L	64.4 ± 14.8	63.1 ± 17.5	64.4 ± 16.7	60.3 ± 21.4	63.2 ± 16.8	63.5 ± 16.3	61.8 ± 17.3	60.8 ± 14.1

Table **4-1**: Results in F1-score (F1) and classification accuracy (Ac) average across subjects for the Valence (V), Arousal (A), Dominance (D) and Liking (L) categories.

serve that generally, our DSC based approach reaches higher accuracy and F1 score than S-FLEX and MSP, with differences between 5 and 10 points. Nevertheless, both performance measures vary according to the used λ_s/λ_t ratio, which could be an indicator of the implicit spatiotemporal dynamics of the brain networks that appear under each emotional stimuli. For instance, liking reaches the maximum F1 and accuracy rate when the spatial parameter has a greater weight (90:30), which corresponds to just a few significant connections (see Fig. **4-3**). In the other hand, Valence achieves the maximum performance scores when the temporal parameter is greater than the spatial one (30:90), which could indicate that this emotional state present brain connections with strong temporal dynamics. However, for those emotional states (Liking and Valence), the achieved DSC based results do not overcome the EEG-based results, reaching similar accuracy and F1 score values.
In the remaining classes, namely Arousal and Dominance, the proposed approach clearly exceeds the comparing approaches. Specifically, DSC achieves 5 points greater than EEG in Arousal both in 90:30 and 90:90 ratios. This could be an indicator that there is a compromise between spatial and temporal dynamics present under this emotional stimuli, as can be seen in Figs. **4-3** and **4-4**. Finally, for Dominance, our approach with 90:90 ratio overcomes the EEG-based results for 2 points.
Summarizing, the DSC(90:90) based approach reaches the better results. In this regard, although for some cases this ratio does not achieve the maximum accuracy and F1 score values, this compromise between the spatial and temporal patterns of brain activity always is close to the higher values.

4.5 Discussion

We proposed a new source connectivity approach explicitly including spatiotemporal information of the neural activity extracted from M/EEG recordings. Particularly, the proposed source connectivity approach is an extension of our DSC based brain mapping approach, hence it allows to encode the source non-stationarities to improve the source connectivity performance. Our approach comprises three critical stages: *i*) ROI identification, *ii*) Estimation of ROI time courses, and *iii*) Assessment of functional connectivity between pairs of ROIs.

ROI identification: As a rule, the estimated source activity spreads over the entire cortical mesh so that the identification of spatially neighboring regions (that is, the ROI set) must be carefully performed. In turn, all ROIs must be densely allocated within small clusters to encode the spatial inhomogeneity of brain activity so that they can be extracted by applying, at least, one of the following principles: By incorporating the prior knowledge of their well-studied participation in experimental tasks [26], or by tracking the structural connectivity networks [62]. Here, unlike traditional source connectivity methods that first estimate the cortical sources and then define the set of ROIs to estimate their time courses, our approach

first define ROIs, which are compact neighboring regions, through all the cortical surface to later estimate the activity inside each ROI based on the measured EEG data. Consequently, the active ROIs are estimated based solely in the available data. The main advantage of this strategy is that allows selecting compact shape clusters as ROIs, which are more similar to real scenarios. However, if needed, this approach also allows creating ROIs as predefined Brodmann areas, or as areas based on fMRI studies.

Estimation of ROI time courses: There are several strategies to compute the time course that define the activity inside each individual ROI. The most used strategies are *i*) To average the time courses of all the dipoles belonging to a specific ROI, or *ii*) To select the time course of the dipole with the highest energy [28]. Nevertheless, each ROI may contain dipoles with different dynamics, so that the average may yield a blurred or noisy time course representing the temporal behavior of such region. Additionally, the dipole with the highest energy will not correctly comprise the temporal dynamic of the entire region.

To cope the above-mentioned issues, we proposed a new approach for estimating the particular dynamics of each ROI, in such a way, that a single time-courses can capture the time variant information of each particular area. In this regard, the estimation of the time varying parameters proposed in the DSC source estimation approach (see Eq. (4-1)), provides an estimation of the ROI time courses taking into account the spatiotemporal dynamics of M/EEG data. Furthermore, the ratio between the spatial and temporal regularization parameters helps to syntonize the algorithm depending on how strong are the temporal dynamics of the data. For instance, we have shown that equating both parameters, we are able to correctly identify the dynamics of emotional states.

Finally, comparing the obtained results with all the tested methods, this step has been the most determining one to correctly perform the source connectivity analysis. This can be evidenced due to all the tested methods use the same ROIs, hence, variations in connectivity patterns, and consequently, in the performance of the emotion classification are directly related to the accurate estimation of the ROI time courses.

Assessment of pairwise connectivity between ROIs: Several measures have been designed to measure the interaction between distant brain areas [22]. Here, all the effort was carried out in the previous steps, hence, we have used one of the most common functional connectivity measures, namely, the *Magnitude Squared Coherence*. We have selected this measure because it allows computing interactions over predefined frequency ranks and it also has been used before for emotional states processing [58]. Although we have reached good performance results, one of the promising alternatives of improvement is to employ a connectivity measure that allows describing with more confidence the time-varying dynamics of the brain networks.

Emotion discrimination based on source connectivity analysis: Lastly, we used the connectivity patterns as features to discriminate between emotions. To carried out a fair comparison, we compute connectivity patterns from all the tested brain mapping methods, but also from raw EEG data, as proposed in [58]. Then, the discrimination was done in two different ways: *i*) By looking for the most significant connections to discriminate between classes, and *ii*) By training an SVM classifier. We have shown that although all tested methods find similar significant connections, differences in classification accuracies and F1 scores reach up to ten points.

In most of the cases, our DSC(90:90) based method reached outstanding results. In this regard, comparing this method against S-FLEX and MSP, results are significantly greater for all the tested emotions. Additionally, although the EEG-based connectivity also reaches good classification performance, the DSC(90:90) is, in the worst case, equal, but also in some cases (Arousal and Dominance, specifically) better.

Finally, notice that we carried out the binary classification as the only one reported in the literature for emotion recognition. However, the use of hard thresholding algorithms for binarizing a label set leads to losing most of the emotional richness. Moreover, the scores near the midpoints and extreme values may have different implications. Therefore, other strategies of labeling should be considered to capture better the richness of emotion dimensions (like the use of regressions).

5 Final Remarks

5.1 General Conclusions and Main Contributions

Design of a brain activity estimation algorithm including spatiotemporal constraints

In Chapter 3 we introduced a constrained M/EEG inverse solution namely *Dinamic Sparse Coding (DSC)* that includes spatiotemporal constraints for improving the reconstruction accuracy of neural activity obtained from M/EEG recordings through a dynamic small and locally smooth spatial patches that vary smoothly over time, yielding sparse and time homogeneous brain activity reconstructions. We tested the DSC in several simulated and real-world applications. For simulations, in the two experiments designed we have shown that DSC improves the temporal accuracy of brain activity reconstruction whereas the spatial accuracy is comparable with state of the art algorithms. For real data we tested our approach on ADHD data. As a result, our proposed method is suitable for reconstructing Evoked Response Potentials, and yields physiologically meaningful solutions: spatially coherent activity and smooth time series. Also, we tested our approach in DEAP data resulting in that our method leads to find significant differences in the low and high values of the considered emotion(valence, arousal, dominance, liking). In general, the implementation of DSC promotes focal and spatially smooth solutions being able to describe non-stationay brain activations.
As future work, we will consider introducing a weighing in the fusion restriction of the DSC to keep track of the dynamics in the latent states.

Tunning of regularization parameters

In Chapter 3 we introduced two optimization strategies for tunning of regularization parameters in DSC, namely, the *Sparsest possible solution* and the *Residual norm criterion*, these optimization methods based their operation on the selection of different ratios reaching a trade-off between the spatial resolution and the temporal resolution, we tested the syntonization of the regularization parameters in the DSC approach in two ways. First, we set different ratios from the solely spatial regularization (Lasso) until the entirely temporal structure reconstruction (Fusion) given as results suitable accuracy with the two optimization strategies in the DSC considering at the same time spatial and temporal restrictions

compared with methods in the state-of-art. Second, we compared the DSC with the *Sparsest possible solution* and different ratios against several inverse method in the emotion-base database resulting in a DSC competitive with the state-of-art algorithms. In general, the two restrictions in DSC give us the freedom to move between the spatial and temporal reconstructions, which is of great importance depending on the application chosen and the specific data in hand. Also, the two tunning methods boost the competitiveness of DSC allowing seek the best possible parameters for implementation given a plus to the *Sparsest possible solution* due to lower computational cost.
As future work, the discussion of the tuning of the parameters in regularization methods is not an easy task which remains open, for this reason, it is necessary to deepen the issue further and try to find better methods.

Development of a source connectivity analysis method

Finally, in Chapter 4 we introduced a source connectivity method that explicitly includes the spatiotemporal dynamics of brain activity. Unlike most of the state-of-art source connectivity methods, we emphasize in estimating the ROIs time courses, as they are the basis of the further connectivity analysis. We tested the proposed method discriminating emotional stages in the emotion-base database. Results showed that the discussed DSC based approach improve the source connectivity based on the state-of-art methods with performance variable depending the spatial-temporal ratio. Additionally, the proposed method either overcomes or al least reach similar results compared against the ones obtained with sensor level based connectivity, depending on the spatiotemporal dynamics of brain activity.
As future work, we plan to employ other connectivity measures that allow describing with more confidence the time-varying dynamics of the brain networks, also, use other strategies to labeling the DEAP database.

5.2 Future work

Besides the method-specific analyses proposed above as future work, more general topics should also be consider:

Non-Gaussian assumptions: The mathematical framework presented in this thesis was grounded on Gaussian assumptions. Nevertheless, though this assumption showed to be enough to achieve outstanding results, some studies in the last years suggest that data recorded from M/EEG follows non-Gaussian distributions [63]. In this regard, the mathematical formulation in Chapter 3 could be easily extended and implemented with non-Gaussian assumptions using *Information Theoretic Learning (ITL)* [64]. In this way, the cost function of Eq. (3-2), which uses only second order statistics could be modified by more

robust functionals as the Information Potential or even the correntropy. Also, the regularization terms, specifically the one encouraging sparsity, could be smoothed with divergences to facilitate its optimization.

Interpretability of the M/EEG inverse problem solution: Typically, M/EEG-based brain mapping solutions provide valuable information about active brain areas. In this regard, one of the contributions of this thesis was to analyze the temporal information provided by M/EEG signals could be used to improve the decoding of the spatiotemporal dynamics of neural activity. Also, we introduced how such temporal information could also improve a further connectivity analysis, which is highly influenced by the decoded neural dynamics. In this regard, we also propose as future work to use the proposed connectivity analysis technique to elucidate differentiable patterns between controls and subjects suffering from several neurological disorders, as middle cognitive impairment, Alzheimer, among others.

Bibliography

[1] S. Baillet, J. C. Mosher, and R. M. Leahy, "Electromagnetic Brain Mapping," *Signal Processing Magazine, IEEE*, vol. 18, no. November, pp. 14 –30, 2001.

[2] M. A. Jatoi, N. Kamel, A. S. Malik, I. Faye, and T. Begum, "A survey of methods used for source localization using eeg signals," *Biomedical Signal Processing and Control*, vol. 11, pp. 42–52, 2014.

[3] A. W. Toga and J. C. Mazziotta, *Brain Mapping: The Methods: The Methods*. Academic press, 2002.

[4] H. Hallez, B. Vanrumste, R. Grech, J. Muscat, W. De Clercq, A. Vergult, Y. D'Asseler, K. P. Camilleri, S. G. Fabri, S. Van Huffel *et al.*, "Review on solving the forward problem in eeg source analysis," *Journal of neuroengineering and rehabilitation*, vol. 4, no. 1, p. 1, 2007.

[5] R. Grech, T. Cassar, J. Muscat, K. Camilleri, S. Fabri, M. Zervakis, P. Xanthopoulos, V. Sakkalis, and B. Vanrumste, "Review on solving the inverse problem in eeg source analysis," *Journal of NeuroEngineering and Rehabilitation*, vol. 5, no. 25, pp. 792 –800, june 2008.

[6] M. Vega-Hernández, E. Martínez-Montes, J. M. Sánchez-Bornot, A. Lage-Castellanos, and P. A. Valdés-Sosa, "Penalized least squares methods for solving the eeg inverse problem," *Statistica Sinica*, pp. 1535–1551, 2008.

[7] R. D. Pascual-Marqui, "Review of methods for solving the EEG inverse problem," *International journal of bioelectromagnetism*, vol. 1, no. 1, pp. 75–86, 1999.

[8] R. D. Pascual-Marqui, C. M. Michel, and D. Lehmann, "Low resolution electromagnetic tomography: a new method for localizing electrical activity in the brain," *International Journal of psychophysiology*, vol. 18, no. 1, pp. 49–65, 1994.

[9] A. Gramfort, D. Strohmeier, J. Haueisen, M. S. Hämäläinen, and M. Kowalski, "Time-frequency mixed-norm estimates: Sparse m/eeg imaging with non-stationary source activations," *NeuroImage*, vol. 70, pp. 410–422, 2013.

[10] I. F. Gorodnitsky, J. S. George, and B. D. Rao, "Neuromagnetic source imaging with focuss: a recursive weighted minimum norm algorithm," *Electroencephalography and clinical Neurophysiology*, vol. 95, no. 4, pp. 231–251, 1995.

[11] S. Haufe, R. Tomioka, T. Dickhaus, C. Sannelli, B. Blankertz, G. Nolte, and K.-R. Müller, "Large-scale eeg/meg source localization with spatial flexibility," *NeuroImage*, vol. 54, no. 2, pp. 851–859, 2011.

[12] K. Friston, L. Harrison, J. Daunizeau, S. Kiebel, C. Phillips, N. Trujillo-Barreto, R. Henson, G. Flandin, and J. Mattout, "Multiple sparse priors for the m/eeg inverse problem," *NeuroImage*, vol. 39, no. 3, pp. 1104–1120, 2008.

[13] D. Wipf and S. Nagarajan, "A unified bayesian framework for meg/eeg source imaging," *Neuroimage*, vol. 44, no. 3, pp. 947–966, 2009.

[14] J. P. Owen, D. P. Wipf, H. T. Attias, K. Sekihara, and S. S. Nagarajan, "Performance evaluation of the champagne source reconstruction algorithm on simulated and real m/eeg data," *Neuroimage*, vol. 60, no. 1, pp. 305–323, 2012.

[15] U. Schmitt and A. K. Louis, "Efficient algorithms for the regularization of dynamic inverse problems: I. theory," *Inverse Problems*, vol. 18, no. 3, pp. 645–660, 2002.

[16] U. Schmitt, A. Louis, C. Wolters, and M. Vauhkonen, "Efficient algorithms for the regularization of dynamic inverse problems: II. Applications," *Inverse Problems*, vol. 18, no. 3, p. 659, 2002.

[17] A. Galka, O. Yamashita, T. Ozaki, R. Biscay, and P. Valdés-Sosa, "A solution to the dynamical inverse problem of EEG generation using spatiotemporal Kalman filtering." *NeuroImage*, vol. 23, no. 2, pp. 435–53, 2004.

[18] M. J. Barton, P. a. Robinson, S. Kumar, A. Galka, H. F. Durrant-Whyte, J. Guivant, and T. Ozaki, "Evaluating the performance of Kalman-filter-based EEG source localization." *IEEE transactions on bio-medical engineering*, vol. 56, no. 1, pp. 122–36, Jan. 2009.

[19] C. Phillips, M. D. Rugg, and K. J. Friston, "Anatomically informed basis functions for eeg source localization: combining functional and anatomical constraints," *NeuroImage*, vol. 16, no. 3, pp. 678–695, 2002.

[20] ——, "Systematic regularization of linear inverse solutions of the EEG source localization problem," *NeuroImage*, vol. 17, no. 1, pp. 287 – 301, 2002.

[21] M. E. Raichle, "A paradigm shift in functional brain imaging," *The Journal of Neuroscience*, vol. 29, no. 41, pp. 12 729–12 734, 2009.

[22] J.-M. Schoffelen and J. Gross, "Source connectivity analysis with meg and eeg," *Human brain mapping*, vol. 30, no. 6, pp. 1857–1865, 2009.

[23] M. J. Brookes, G. C. O'Neill, E. L. Hall, M. W. Woolrich, A. Baker, S. P. Corner, S. E. Robson, P. G. Morris, and G. R. Barnes, "Measuring temporal, spectral and spatial changes in electrophysiological brain network connectivity," *Neuroimage*, vol. 91, pp. 282–299, 2014.

[24] L. Astolfi, F. Cincotti, D. Mattia, S. Salinari, C. Babiloni, A. Basilisco, P. M. Rossini, L. Ding, Y. Ni, B. He, M. G. Marciani, and F. Babiloni, "Estimation of the effective and functional human cortical connectivity with structural equation modeling and directed transfer function applied to high-resolution EEG," *Magnetic Resonance Imaging*, vol. 22, no. 10, pp. 1457 – 1470, 2004.

[25] L. Astolfi, F. Cincotti, D. Mattia, C. Babiloni, F. Carducci, A. Basilisco, P. Rossini, S. Salinari, L. Ding, Y. Ni, B. He, and F. Babiloni, "Assessing cortical functional connectivity by linear inverse estimation and directed transfer function: simulations and application to real data," *Clinical Neurophysiology*, vol. 116, no. 4, pp. 920 – 932, 2005.

[26] F. Babiloni, F. Cincotti, C. Babiloni, F. Carducci, D. Mattia, L. Astolfi, A. Basilisco, P. Rossini, L. Ding, Y. Ni, J. Cheng, K. Christine, J. Sweeney, and B. He, "Estimation of the cortical functional connectivity with the multimodal integration of high-resolution EEG and fMRI data by directed transfer function," *NeuroImage*, vol. 24, no. 1, pp. 118 – 131, 2005.

[27] M. J. Brookes, J. R. Hale, J. M. Zumer, C. M. Stevenson, S. T. Francis, G. R. Barnes, J. P. Owen, P. G. Morris, and S. S. Nagarajan, "Measuring functional connectivity using MEG: methodology and comparison with fcMRI," *Neuroimage*, vol. 56, no. 3, pp. 1082–1104, 2011.

[28] M. Hassan, O. Dufor, I. Merlet, C. Berrou, and F. Wendling, "Eeg source connectivity analysis: from dense array recordings to brain networks," *PloS one*, vol. 9, no. 8, p. e105041, 2014.

[29] M. Grosse-wentrup, "Understanding brain connectivity patterns during motor imagery for brain-computer interfacing," in *Advances in Neural Information Processing Systems 21*, D. Koller, D. Schuurmans, Y. Bengio, and L. Bottou, Eds. Curran Associates, Inc., 2009, pp. 561–568.

[30] V. Litvak and K. Friston, "Electromagnetic source reconstruction for group studies," *Neuroimage*, vol. 42, no. 4, pp. 1490–1498, 2008.

[31] R. N. Henson, G. Flandin, K. J. Friston, and J. Mattout, "A Parametric Empirical Bayesian framework for fMRI-constrained MEG/EEG source reconstruction," *Human brain mapping*, vol. 31, no. 10, pp. 1512–1531, 2010.

[32] R. N. Henson, D. G. Wakeman, V. Litvak, and K. J. Friston, "A parametric empirical Bayesian framework for the EEG/MEG inverse problem: generative models for multi-subject and multi-modal integration," *Front. Hum. Neurosci*, vol. 5, no. 76, pp. 10–3389, 2011.

[33] J. Nocedal and S. J. Wright, *Numerical Optimization*, 2nd ed. New York: Springer, 2006.

[34] R. Tibshirani, "Regression shrinkage and selection via the lasso," *Journal of the Royal Statistical Society. Series B (Methodological)*, pp. 267–288, 1996.

[35] K. Uutela, M. Hämäläinen, and E. Somersalo, "Visualization of magnetoencephalographic data using minimum current estimates," *NeuroImage*, vol. 10, no. 2, pp. 173–180, 1999.

[36] S. Haufe, V. V. Nikulin, A. Ziehe, K.-R. Müller, and G. Nolte, "Combining sparsity and rotational invariance in eeg/meg source reconstruction," *NeuroImage*, vol. 42, no. 2, pp. 726–738, 2008.

[37] P. Belardinelli, E. Ortiz, G. Barnes, U. Noppeney, and H. Preissl, "Source Reconstruction Accuracy of MEG and EEG Bayesian Inversion Approaches." *PloS one*, vol. 7, no. 12, p. e51985, Dec. 2012.

[38] R. Tibshirani, M. Saunders, S. Rosset, J. Zhu, and K. Knight, "Sparsity and smoothness via the fused lasso," *Journal of the Royal Statistical Society: Series B (Statistical Methodology)*, vol. 67, no. 1, pp. 91–108, 2005.

[39] S. Castaño-Candamil, J. Höhne, J.-D. Martínez-Vargas, X.-W. An, G. Castellanos-Domínguez, and S. Haufe, "Solving the eeg inverse problem based on space–time–frequency structured sparsity constraints," *NeuroImage*, vol. 118, pp. 598–612, 2015.

[40] G. E, J. Martinez-Vargas, and G. Castellanos-Dominguez, "Reconstruction of neural activity from EEG data using dynamic spatio-temporal constraints," *International Journal of Neural Systems*, 2016.

[41] X. Chen, S. Kim, Q. Lin, J. G. Carbonell, and E. P. Xing, "Graph-Structured Multi-task Regression and an Efficient Optimization Method for General Fused Lasso," *ArXiv e-prints*, May 2010.

[42] C. Rakesh, "A hierachical dynamic model for object recognition," Ph.D. dissertation, University of Florida, 2013.

[43] Y. Nesterov, "Smooth minimization of non-smooth functions," *Mathematical Programming*, vol. 103, no. 1, pp. 127–152, 2005.

[44] T. R. Mullen, C. A. Kothe, Y. M. Chi, A. Ojeda, T. Kerth, S. Makeig, T.-P. Jung, and G. Cauwenberghs, "Real-time neuroimaging and cognitive monitoring using wearable dry eeg," *Biomedical Engineering, IEEE Transactions on*, vol. 62, no. 11, pp. 2553–2567, 2015.

[45] P. van Mierlo, E. Carrette, H. Hallez, K. Vonck, D. V. Roost, P. Boon, and S. Staelens, "Accurate epileptogenic focus localization through time-variant functional connectivity analysis of intracranial electroencephalographic signals," *NeuroImage*, vol. 56, no. 3, pp. 1122 – 1133, 2011. [Online]. Available: http://www.sciencedirect.com/science/article/pii/S1053811911001479

[46] U. Volpe, A. Mucci, P. Bucci, E. Merlotti, S. Galderisi, and M. Maj, "The cortical generators of p3a and p3b: a loreta study," *Brain research bulletin*, vol. 73, no. 4, pp. 220–230, 2007.

[47] S. Koelstra, C. Muhl, M. Soleymani, J.-S. Lee, A. Yazdani, T. Ebrahimi, T. Pun, A. Nijholt, and I. Patras, "Deap: A database for emotion analysis ;using physiological signals," *Affective Computing, IEEE Transactions on*, vol. 3, no. 1, pp. 18–31, Jan 2012.

[48] I. Siegert, R. Bock, B. Vlasenko, D. Philippou-Hubner, and A. Wendemuth, "Appropriate emotional labelling of non-acted speech using basic emotions, geneva emotion wheel and self assessment manikins," in *Multimedia and Expo (ICME), 2011 IEEE International Conference on*, Barcelona, July 2011, pp. 1–6.

[49] A. F. Arnsten, L. Scahill, and R. L. Findling, "Alpha-2 adrenergic receptor agonists for the treatment of attention-deficit/hyperactivity disorder: emerging concepts from new data," *Journal of child and adolescent psychopharmacology*, vol. 17, no. 4, pp. 393–406, 2007.

[50] A. F. Arnsten, "The use of α-2a adrenergic agonists for the treatment of attention-deficit/hyperactivity disorder," *Expert review of neurotherapeutics*, vol. 10, no. 10, pp. 1595–1605, 2010.

[51] J. Prince, "Catecholamine dysfunction in attention-deficit/hyperactivity disorder: an update," *Journal of clinical psychopharmacology*, vol. 28, no. 3, pp. S39–S45, 2008.

[52] A. Vance, T. Silk, M. Casey, N. Rinehart, J. Bradshaw, M. Bellgrove, and R. Cunnington, "Right parietal dysfunction in children with attention deficit hyperactivity disorder, combined type: a functional mri study," *Molecular psychiatry*, vol. 12, no. 9, pp. 826–832, 2007.

[53] S. Cortese, C. Kelly, C. Chabernaud, E. Proal, A. Di Martino, M. P. Milham, and F. X. Castellanos, "Toward systems neuroscience of adhd: a meta-analysis of 55 fmri studies," *American Journal of Psychiatry*, 2012.

[54] H. Hart, J. Radua, T. Nakao, D. Mataix-Cols, and K. Rubia, "Meta-analysis of functional magnetic resonance imaging studies of inhibition and attention in attention-deficit/hyperactivity disorder: exploring task-specific, stimulant medication, and age effects," *JAMA psychiatry*, vol. 70, no. 2, pp. 185–198, 2013.

[55] S. J. Johnstone, R. J. Barry, and A. R. Clarke, "Ten years on: a follow-up review of erp research in attention-deficit/hyperactivity disorder," *Clinical Neurophysiology*, vol. 124, no. 4, pp. 644–657, 2013.

[56] L. Astolfi, F. Cincotti, D. Mattia, F. De Vico Fallani, A. Tocci, A. Colosimo, S. Salinari, M. Marciani, W. Hesse, H. Witte, M. Ursino, M. Zavaglia, and F. Babiloni, "Tracking the time-varying cortical connectivity patterns by adaptive multivariate estimators," *Biomedical Engineering, IEEE Transactions on*, vol. 55, no. 3, pp. 902–913, March 2008.

[57] L. Nummenmaa, E. Glerean, M. Viinikainen, I. P. Jääskeläinen, R. Hari, and M. Sams, "Emotions promote social interaction by synchronizing brain activity across individuals," *Proceedings of the National Academy of Sciences*, vol. 109, no. 24, pp. 9599–9604, 2012.

[58] R. Gupta, Y.-J. Hur, and N. Lavie, "Distracted by pleasure: Effects of positive versus negative valence on emotional capture under load." *Emotion*, vol. 16, no. 3, p. 328, 2016.

[59] S. Haufe, V. V. Nikulin, K.-R. Müller, and G. Nolte, "A critical assessment of connectivity measures for EEG data: A simulation study," *NeuroImage*, vol. 64, pp. 120 – 133, 2013.

[60] N. Srinivasan, "Cognitive neuroscience of creativity: Eeg based approaches," *Methods*, vol. 42, no. 1, pp. 109–116, 2007.

[61] J. I. Padilla-Buritica, J. D. Martinez-Vargas, and G. Castellanos-Dominguez, "Emotion discrimination using spatially compact regions of interest extracted from imaging eeg activity," *Frontiers in Computational Neuroscience*, vol. 10, p. 55, 2016.

[62] J. A. Pineda-Pardo, R. Bruña, M. Woolrich, A. Marcos, A. C. Nobre, F. Maestú, and D. Vidaurre, "Guiding functional connectivity estimation by structural connectivity in meg: an application to discrimination of conditions of mild cognitive impairment," *NeuroImage*, vol. 101, pp. 765 – 777, 2014.

[63] H. R. Mohseni, M. L. Kringelbach, M. W. Woolrich, A. Baker, T. Z. Aziz, and P. Probert-Smith, "Non-gaussian probabilistic MEG source localisation based on kernel density estimation," *NeuroImage*, vol. 87, pp. 444–464, 2014.

[64] J. C. Principe, *Information theoretic learning: Renyi's entropy and kernel perspectives*. Springer Science & Business Media, 2010.